Investigation of Dynamic Fibrils in H-alpha 6563 and Ca II 8542

Elisabeth Helen Fjeldsbø Jordahl
Master thesis
Institute of Theoretical Astrophysics
University of Oslo
Norway

June, 2013

Acknowledgments

I would like to thank my supervisor Luc Rouppe van der Voort for all the help and guidance I have received throughout this project, and also for giving me the chance to partake in an observing campaign at La Palma. Definitely something I will remember for the rest of my life.
I would like to thank Eamon Scullion for teaching me a lot while helping me with the summer project, which really got me excited for this thesis.
Many thanks to my parents and aunt for financially backing this thesis, my nephew for being the cutest distraction, and his parents for all the nice dinners and talks.
I would also like to thank my fellow master students for all the laughs, trips, and get-togethers.

Abstract

Dynamic fibrils (DFs) are a subset of dynamic jets in the lower solar atmosphere, that move up and down along magnetic field lines on the solar disk. Jet-like features have been observed at the solar limb for more than one hundred years, so it is important to find out whether the dynamic fibrils have any physical association to the limb features. Recent developments of observational instruments and post-processing imaging techniques have allowed for advances in image resolution, making on-disk features easier to distinguish and investigate.

In this thesis the properties of dynamic fibrils in the chromosphere will be studied through analyzing the spectral lines hydrogen alpha (H-α) and calcium II 8542 (Ca 8542). These two lines sample slightly different layers of the solar atmosphere. The data set under examination was acquired with the CRISP instrument at the Swedish 1-m Solar Telescope (SST) on La Palma. The dynamic fibrils observed in this data set, are obtained from a small active region, that contains small pores with a lot of dynamic activity.

The research of this thesis will be carried out under the assumption that dynamic fibrils move in parabolic paths, like it has been shown from De Pontieu et al. (2007a), Hansteen et al. (2006) and Langangen et al. (2008b). The thesis will expand on the work of De Pontieu et al. (2007a), Langangen et al. (2008b), and Langangen et al. (2008a), since analysis will be done not only for H-α, but also for Ca 8542. The work will follow analysis methods similar to these papers, but optimized for the data set under investigation.

The main goals of this research will be to advance upon what has already been discovered regarding dynamic fibrils, by firstly confirming certain properties, and secondly to investigate their evolution in the two spectral lines.

From a sample of 50 dynamic fibrils, results confirm the parabolic trajectories of the dynamic fibrils, both in H-α and Ca 8542. Their paths appear clearer in H-α, while in Ca 8542 they can appear more diffuse. The mean properties (such as lifetime, maximum height, velocity and deceleration) of the dynamic fibrils are quite similar in both H-α and Ca 8542. It was found that the general properties of

the dynamic fibrils in this study generally agree with what was found in previous studies.

Contents

Chapter 1

Background

1.1 The Sun

Our closest star is about 4.5 $\times 10^9$ years old, has a radius of about $6,96 \times 10^8$ m, and a mass of $1,99 \times 10^{30}$ kg. It has an average distance from the Earth of 1 Astronomical Unit (AU) ($1,5 \times 10^{11}$ m). The ball of gas and plasma is structured with the radiation zone outside the core, the convection zone, and an outer solar atmosphere. The core is where the hydrogen is converted to helium, the nuclear reaction driving the Sun. In the radiation zone, the temperature decreases as the energy from the nuclear reactions is radiated away from the core. In the convection zone, the temperature decreases ever more as the warmer plasma moves outwards towards the surface, and forms convection cells called granules (Kutner 2003; Priest 1982; Schrijver and Zwaan 2008; Stix 2004). For some general background on the basic properties of the Sun, the reader is referred to textbooks like Kutner (2003); Priest (1982); Schrijver and Zwaan (2008); Stix (2004).

1.1.1 Atmosphere

The outer atmosphere of the Sun consists of different layers, where the photosphere is the layer closest to the surface (see Fig. 1.2). Above the photosphere is the chromosphere (see Fig. 1.3), followed by the transition region (see Fig. 1.4), and the corona (see Fig. 1.5 and Fig. 1.6).

The photosphere is named after the Greek word for light, and this layer is where most of the visible light is emitted. It is also where the Sun turns from being opaque to transparent, so the granules on the surface can be seen. They appear as

Figure 1.1: Sunset behind the international Gran Telescopio Canarias (GranTeCan) at an altitude of 2400 m at the Roque de los Muchachos on La Palma. (*Photo: Elisabeth Jordahl*)

bright convection cells side by side, with darker (cooler) intergranular lanes where they meet each other. These granules have a typical size of 1000 km in diameter and can be seen in Fig. 1.2. The temperature minimum of the Sun is located in the photosphere, at around a height of 500 km above the surface. This decreasing temperature with height, along with the outwards decreasing density, causes limb darkening. Limb darkening is the diminished intensity towards the limb of the solar disk, which makes the limb appear darker.

The chromosphere is the layer between the photosphere and the transition region, illustrated in Fig. 1.3, and introduced in detail in section 1.2

The transition region (Fig. 1.4) is where the temperature increases by about three orders of magnitude, and levels out around a few million degrees in the outermost layer, the corona (Latin for crown). Here the solar wind escapes the Sun with about 10^9 kg/s of the solar mass. The corona is quite faint, about one millionth as bright as the photosphere in white light. The density is about two orders of magnitude less, per cubic meter, than that of the photosphere. The coronal loops (see Fig. 1.5 and Fig. 1.6) are exceptions to this density decrease, and usually have a higher density than their surroundings. (Stix 2004; Kutner 2003; Priest 1982).

Figures 1.2 to 1.6 illustrated the different atmospheric regions of the Sun. The images are taken from the data set analyzed in this thesis. The location and orientation of the field of view (FOV) of the observed data set on the solar disk can be seen in Fig. 1.2 and Fig. 1.3. In these figures, Solar X refers to the north-south direction of the disk, while Solar Y refers to the east-west direction. Figures 1.4 to 1.6 shows images, corresponding to the SST data, obtained with the Solar Dynamics Observatory, which is a space-based telescope that has been in operation since

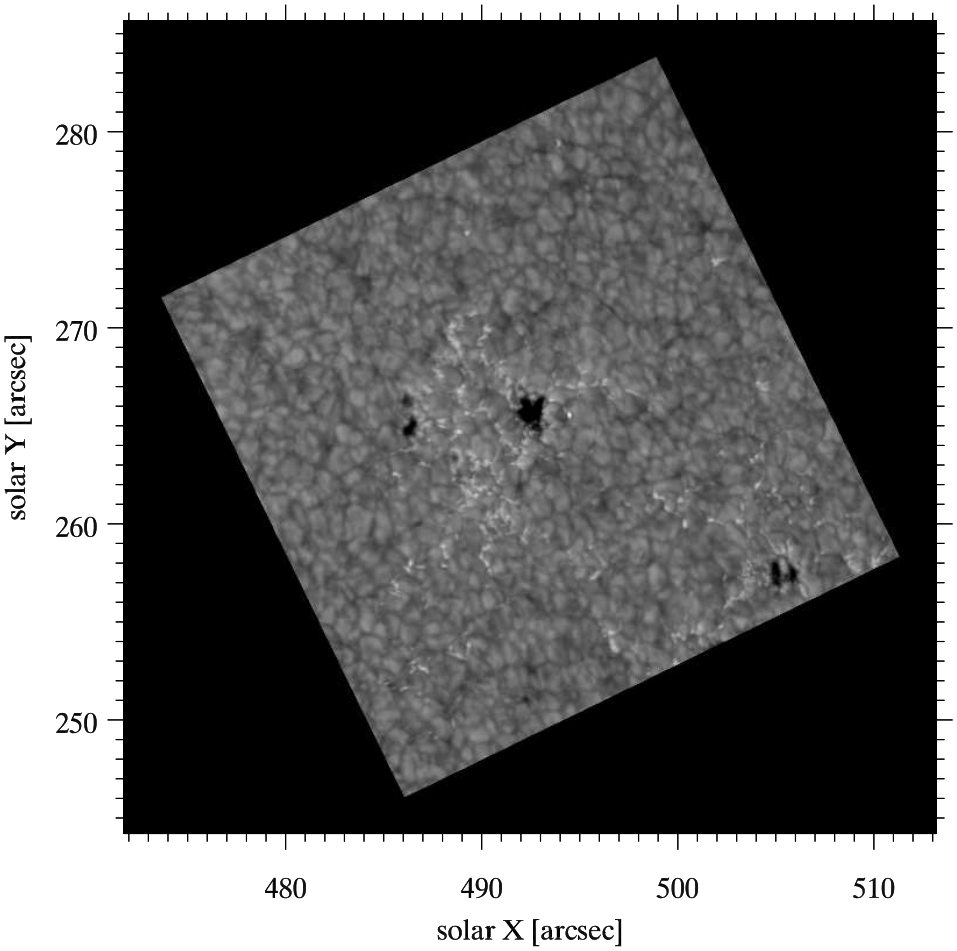

Figure 1.2: CRISP image of the photosphere in the SST 25/06/2010 data set, seen in the H-α continuum. The figure shows how the SST field of view (FOV) in heliocentric coordinates. In the image the granular surface of the Sun can be seen, with a small (unnumbered) active region in the center. A plage region is seen near the center, with a concentration of magnetic bright points and small pores.

mid 2010. SDO contains 4 telescopes, sampling 10 different wavelength bands continuously. The 10 bands are chosen to obtain information from the atmosphere in the temperature range between 6000 and 3×10^6K (Pesnell et al. 2012).

1.2 Chromosphere

The chromosphere is the layer above the photosphere in the outer solar atmosphere, extending about 2000 km upwards. It gets it name from the Greek word chromo, which means colour, due to the pale red glow visible around the lunar limb during

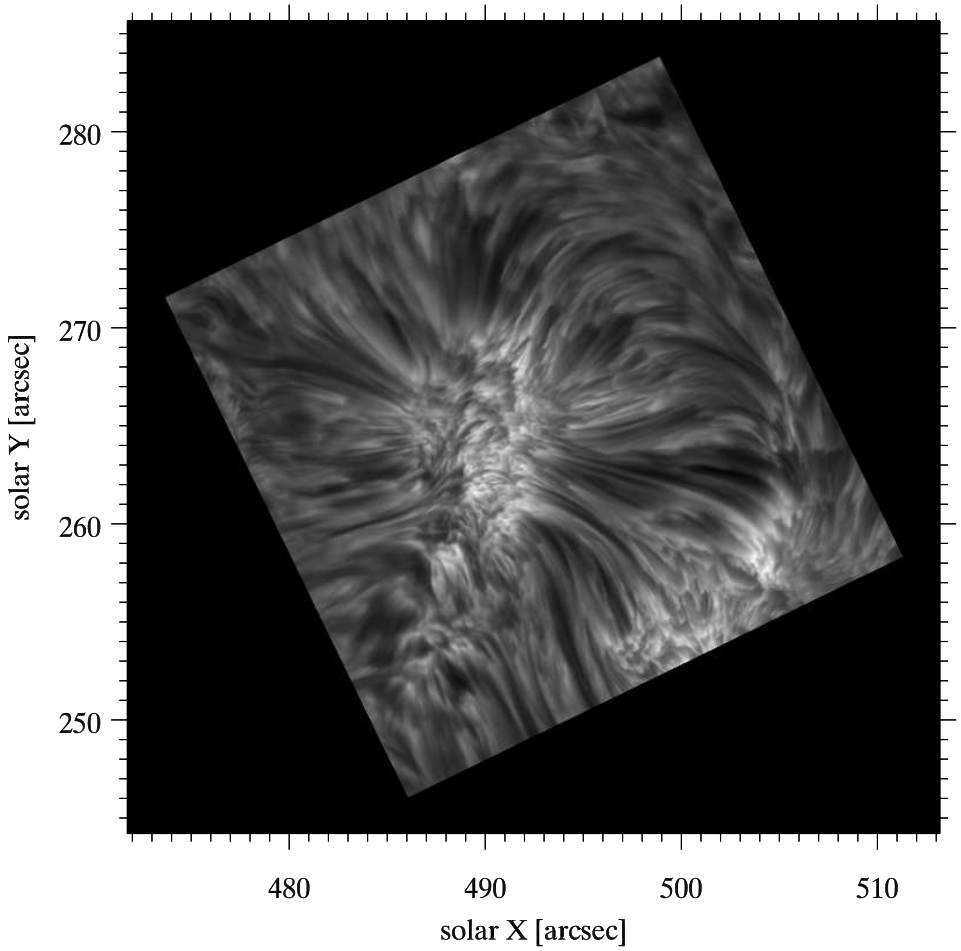

Figure 1.3: CRISP image of the chromosphere in the SST 25/06/2010 data set, seen in H-α line center (6563 Å), with the same field of view (FOV) as Fig. 1.2. In the image, the structure and dynamic features found in the chromosphere can be seen. Dynamic fibrils, that are the main subject of this thesis, are found in the center region.

a solar eclipse, that is mainly caused by the H-α line. The temperature in this layer will increase from a minimum of about 4000 K at the lower boundary, to about 10^4 K, as can be seen in Fig. 1.7.

The chromosphere is highly dynamic, with a lot of elongated gas features, as can be seen by comparing Fig. 1.2 and Fig. 1.3. In the solar atmosphere, the chromosphere is less explored due the complicated physics taking place there. Although it is optically thin for most wavelengths, H-α and Ca 8542 are two of the dominant lines in the visual spectrum forming there. They sample slightly different layers of the solar chromosphere, therefore, observations of these lines make excellent diagnostic tools for probing this atmospheric layer (see e.g Kutner (2003); Langangen

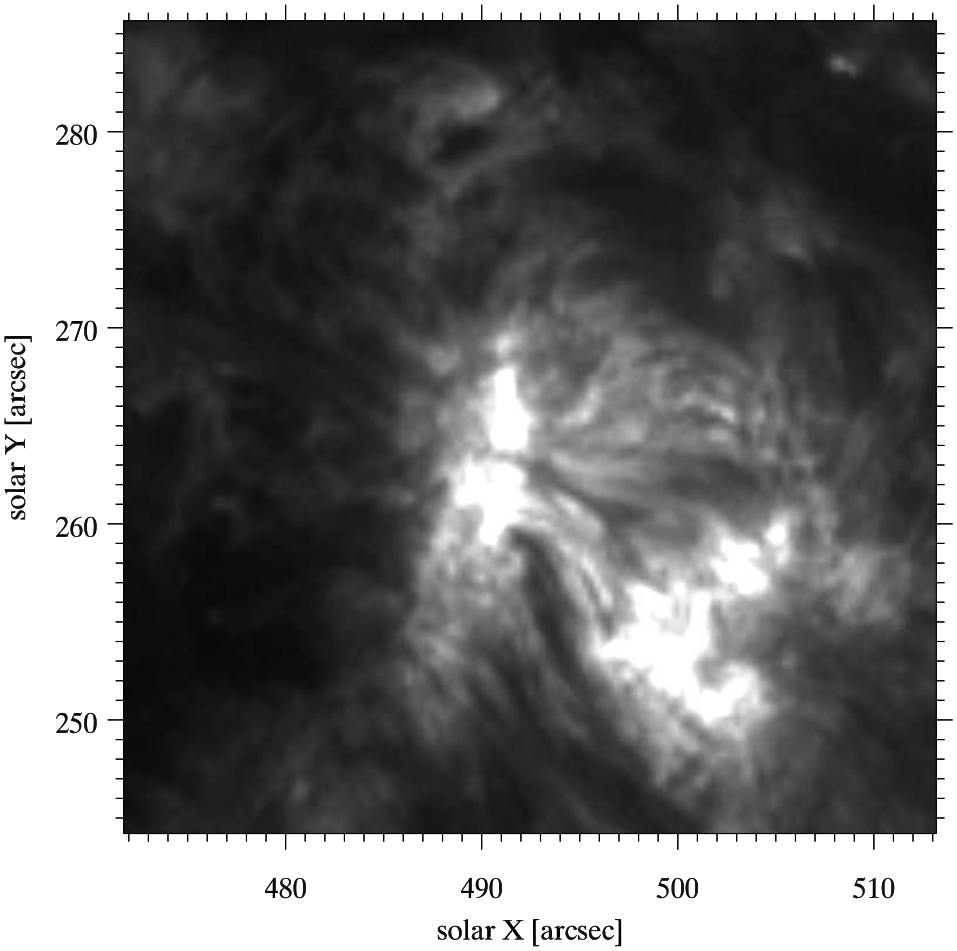

Figure 1.4: SDO He II 304 Å image of the transition region ($\sim 50 \times 10^3$K) of the same region observed with the SST (see Fig. 1.2 and Fig. 1.3). SDO observes the full solar disk continuously at high temporal cadence and has necessarily much lower spatial resolution compared to the SST. The spatial resolution of the SDO is 0.6 arcsec per pixel (Lemen et al. 2012).

et al. (2008b); Leenaarts et al. (2012); Priest (1982); Stix (2004)).

1.2.1 H-α

The H-α line is located at 6563 Å in the electromagnetic spectrum, as seen in red in Fig.1.8. It is the first line in the Balmer series, and a spectral line that results from a radiative transition between levels $n = 3$ and $n = 2$, where n is the principal quantum number. It is one of the most prominent spectral lines originating in the chromosphere. Since hydrogen is the lightest element, it is most

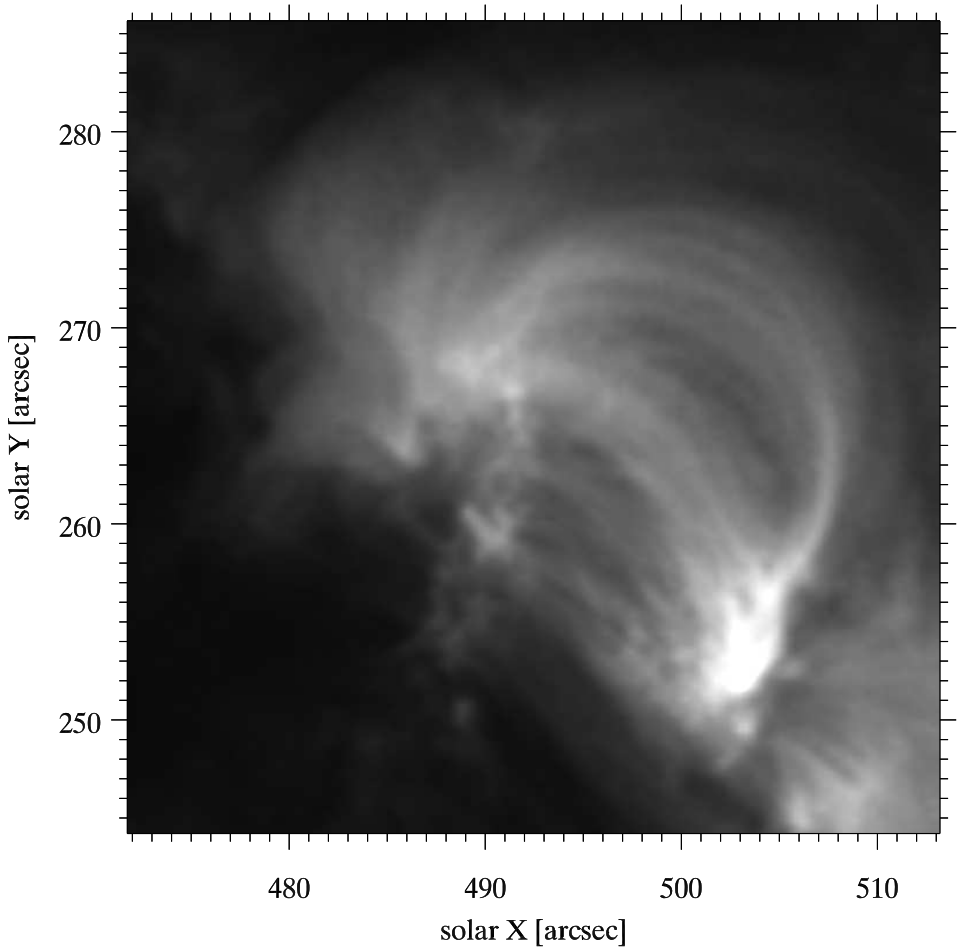

Figure 1.5: SDO Fe IX 171 Å of the "cool" corona ($\sim 600 \times 10^3$K) of the region observed with the SST (see Fig. 1.2 and Fig. 1.3). Some characteristic coronal loops can be seen connecting the two polarities in the small active region.

sensitive to thermal broadening, and therefore has a broad line profile. The H-α line is generally not very sensitive to Doppler shifts, due to the wide line profile, see Fig. 1.9.

Figure 1.10 gives an indication of approximately where the H-α line is formed. The figure shows peaks for different wavelengths, in the line profile, of where they form in the atmosphere. The line core is represented by 0 (blue) and the higher numbers are line indexes which increase towards the wing. The simulations that resulted in Fig. 1.10 and Fig. 1.13 has been done with MULTI (see Carlsson (1986)), for the FALC model atmosphere (see Fontenla et al. (1990)).

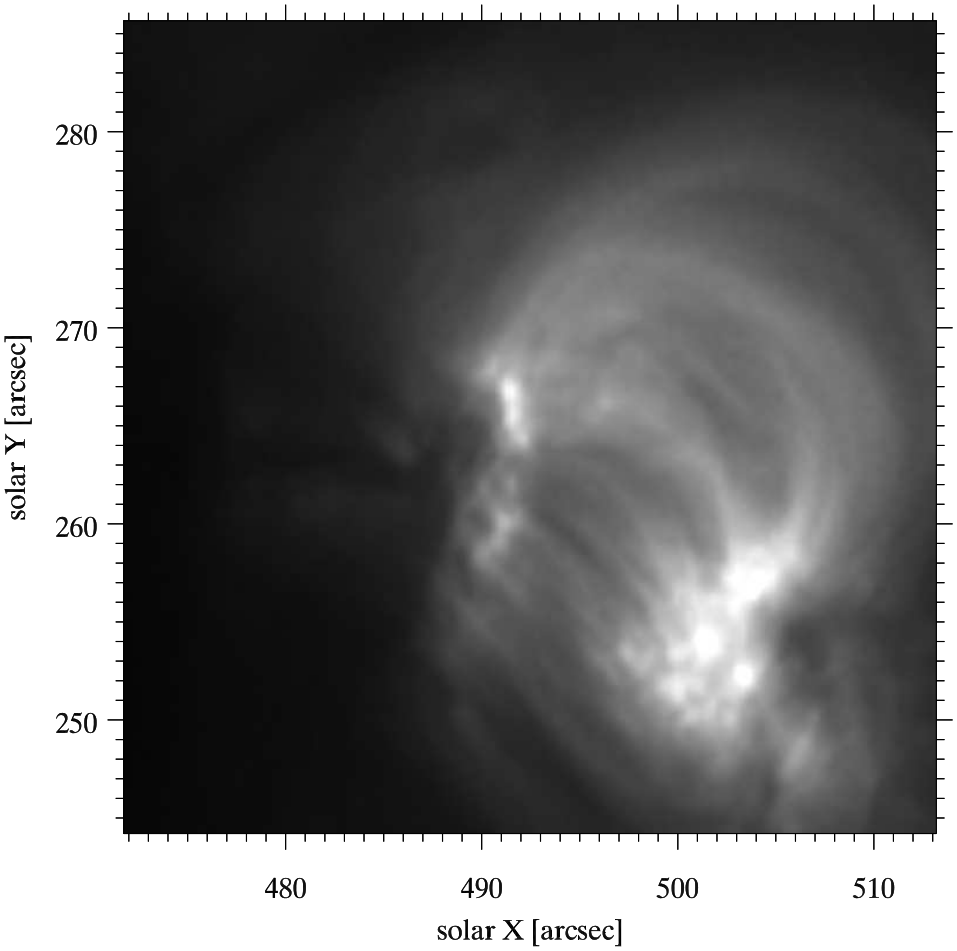

Figure 1.6: SDO Fe XIV 221 Å of the "hot" corona ($\sim 2 \times 10^6$K) of the region observed with the SST (see Fig. 1.2 and Fig. 1.3). Characteristic coronal loops are also seen in this image. This spectral line is often used to study the hot corona in active regions.

1.2.2 Ca 8542

This calcium line is located at 8542 Å, as seen in red in Fig.1.11 . It is a spectral line from singly ionized calcium, and results from a radiative transition between levels $n = 4$ and $n = 3$. The Ca 8542 line is another prominent line originating in the chromosphere, and is quite sensitive to Doppler shifts, due to a narrower line profile compared to H-α, see Fig. 1.12.

In Fig. 1.13, an indication of approximately where the Ca 8542 line is formed is given. This figure, as Fig. 1.10 shows peaks for different wavelengths of where they are formed in the model atmosphere. The line core is represented by 0 (blue) and the higher numbers are line indexes which increase towards the wing. Com-

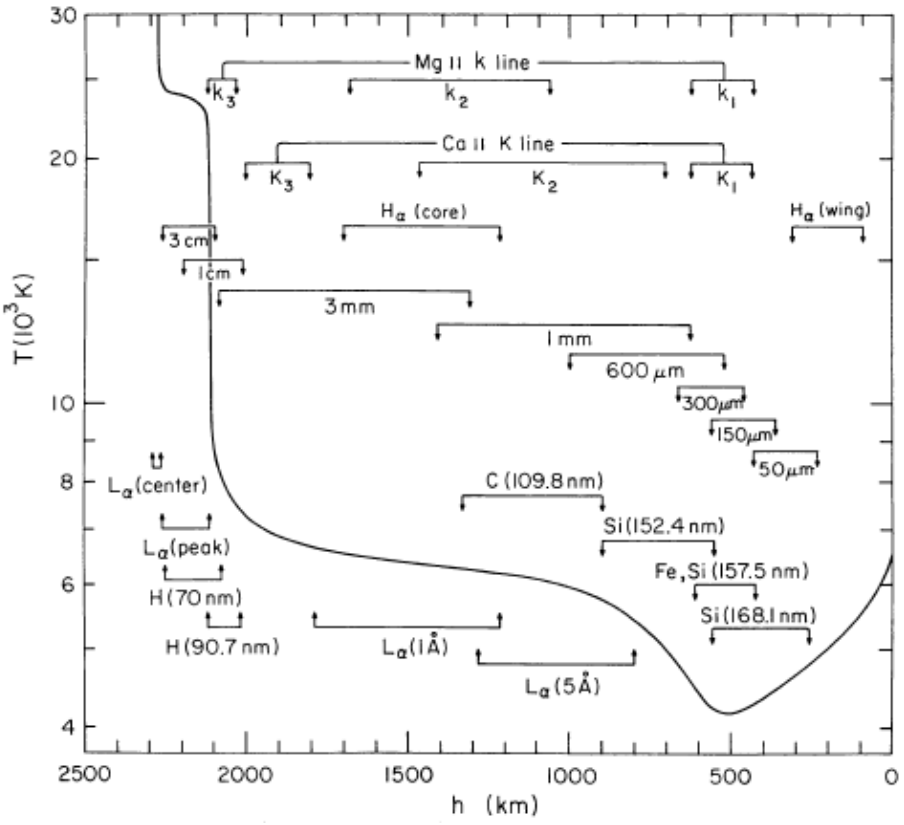

Figure 1.7: Temperature plot of the solar atmosphere from Vernazza et al. (1981). In the plot the formation heights of different spectral lines are indicated.

paring Fig. 1.10 and Fig. 1.13, indicates that the H-α line core is formed higher up in the atmosphere, than the Ca 8542 line core is.

1.2.3 Sunspots

Because the Sun does not rotate like a rigid body, the differential rotation will make the magnetic field twist under the surface. When magnetic flux emerges through the surface, active regions are formed with high magnetic concentrations. Sunspots might form here, and are darker and cooler areas where convection is suppressed by the magnetic field. A sunspot usually consist of a dark umbra (center), with a penumbra around, that is brighter than the umbra, yet generally darker than the surrounding solar surface. The umbra has a size of typically 10 000 to 20 000 km across, and the penumbra a width of 5000 to 7000 km. If a sunspot does not have a penumbra, it is called a pore. The sunspots appear on the solar disk along the sunspot "belt", which is located between $-35°$and $35°$ latitude. The solar activity cycle, from one sunspot minimum to the following minimum, takes on average 11

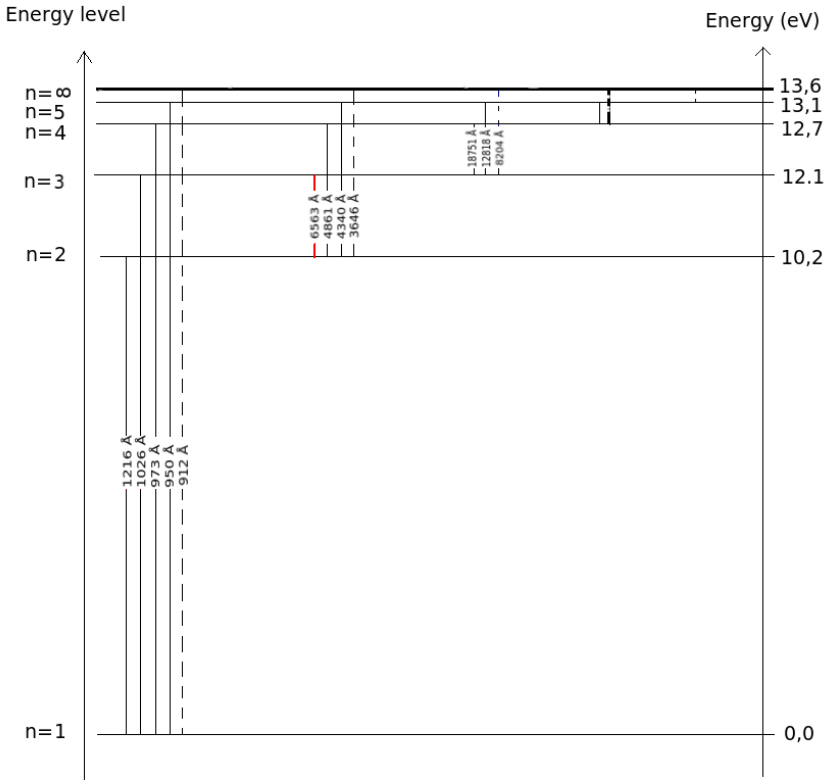

Figure 1.8: Term diagram for hydrogen. 6563 Å line marked in red. Solid lines are bound-bound transitions and dotted lines are bound-free transitions.

years. During this cycle, the sunspots will start out by appearing near the sunspot belt's boundaries and then appear closer to the solar equator as time goes by (Priest 1982; Schrijver and Zwaan 2008; Stix 2004). Smaller concentrations of magnetic field that cover less area than pores, are actually brighter rather than darker than pores and sunspot umbrae. All over the solar surface, these small-scale magnetic concentrations can be found as bright points in inter granular lanes between granules. In active regions, these can be found in large concentrations, often in the trailing part of active regions. These bright areas are commonly referred to as plage (Priest 1982; Schrijver and Zwaan 2008). A plage region can be seen in Fig. 1.2, to the left of the pore at the center of the image.

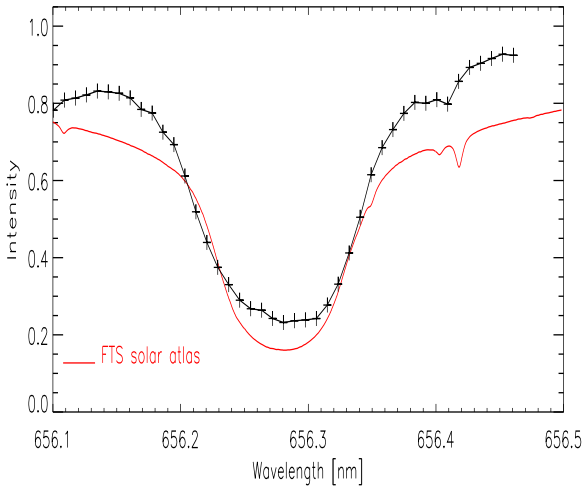

Figure 1.9: Atlas of H-α's line profile (red), along with a actual line profile from the H-α X-T plot (black) in Fig. 2.7. Plus signs mark CRISP wavelength sampling points. The atlas uses normalized intensity. For more on the FTS solar atlas, see Brault and Neckel (1987).

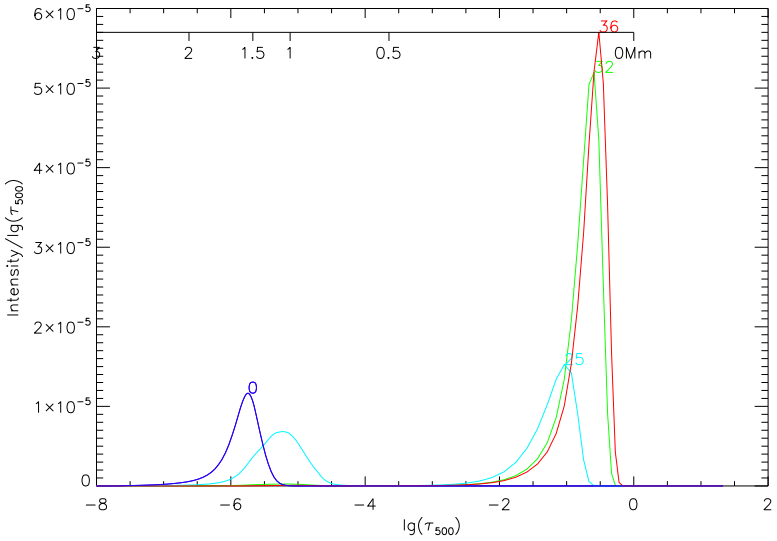

Figure 1.10: Contribution functions indicating formation heights of the H-α line in the solar atmosphere, based on simulations in the FALC model atmosphere. The line core is shown in the blue curve (0), while increasing index of the curves indicate wavelengths farther out in the wing. The simulations have been performed using MULTI.

1.3 Spicules

Spicules were first observed and described by Secchi in 1877 (Secchi 1877). They are dynamic jet-like features, seen at the solar limb. Although spicules have been

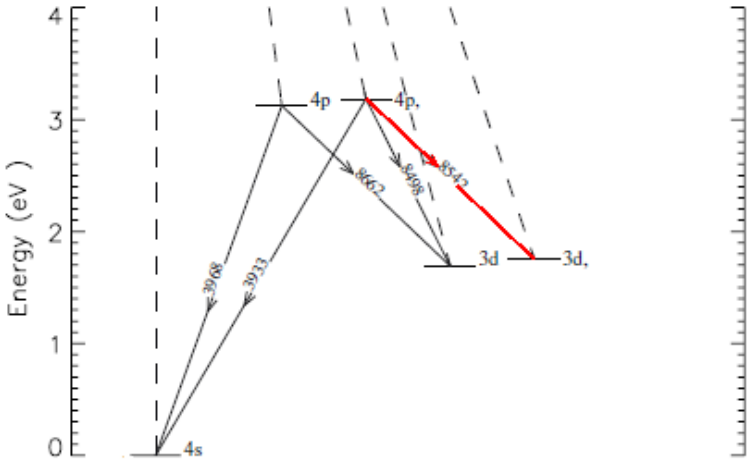

Figure 1.11: Term diagram for calcium II. 8542 line marked in red. Solid lines are bound-bound transitions and dotted lines are bound-free transitions.

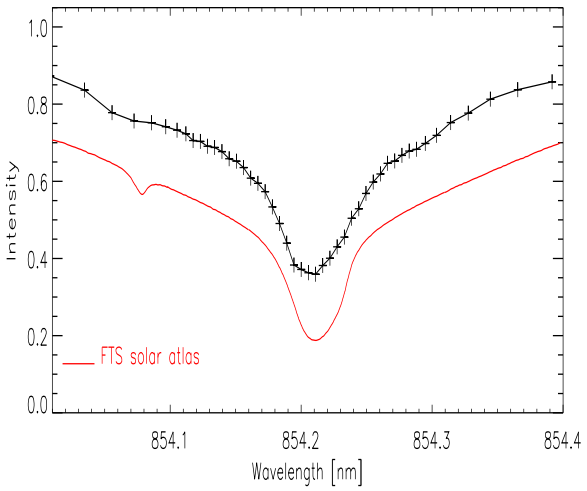

Figure 1.12: Atlas of Ca 8542 line profile (red), along with a actual line profile from the Ca 8542 X-T plot (black) in Fig.2.7. Plus signs mark CRISP wavelength sampling points. The atlas uses normalized intensity. For more on the FTS solar atlas, see Brault and Neckel (1987).

known for more than a hundred years, they have been hard to observe since they are quite thin, short-lived and fast-moving. For a long time, observational techniques were not able to provide information detailed enough to understand their nature. In addition, even though limb observations imply that spicules are present everywhere above the solar surface, it remained unclear what their on-disk counterpart could be. Only recently, the spatial and temporal resolution of observations

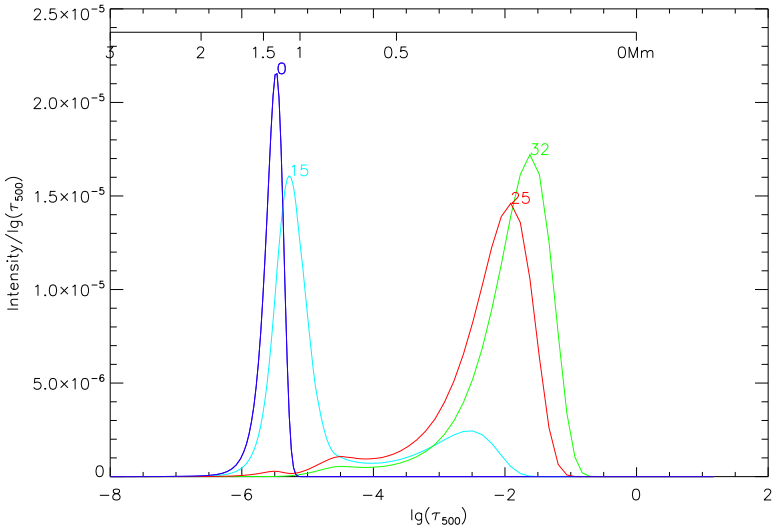

Figure 1.13: Contribution functions indicating formation heights of the Ca 8542 line in the solar atmosphere, based on simulations in the FALC model atmosphere. The line core is shown in the blue curve (0), while increasing index of the curves indicate wavelengths farther out in the wing. The simulations have been performed using MULTI.

have advanced sufficiently to make fundamental progress in the understanding of spicules (De Pontieu et al. 2007b). The launch of the Hinode satellite provided seeing free observations from a telescope with a sufficiently large apperature to resolve the spicules. (For more information on the Hinode satellite see Kosugi et al. (2007)). At the same time, adaptive optics and image restoration techniques evolved enough so that high resolution observations of spicules from the ground became possible. From Hinode observations it has become clear that there are two types of spicules, type I and type II (De Pontieu et al. 2007b). The two types appear to be different, where type I moves up and down and type II moves up and disappear. Type I spicules and the observed on-disk dynamic fibrils (see 1.4) near active regions (AR), seem to have a common origin (De Pontieu et al. 2007b). They both originate due to shock waves in the chromosphere, caused by the leakage of pressure waves along inclined magnetic field lines in the photosphere (De Pontieu et al. 2004, 2007a). For type II spicules it has become clear that rapid blue-shifted excursions (RBEs) are their on-disk counterpart (Rouppe van der Voort et al. 2009).

The lifetimes of the type I spicules are usually within 3 to 7 minutes, where they reach average heights of about 4 to 8 Mm (active regions) (Pereira et al. 2012). Type I spicules move up and down and follow non-ballistic parabolic paths, i.e. their deceleration is not driven by solar gravity (De Pontieu et al. 2007b; Pereira et al. 2012). This behaviour makes type I spicules a lot like the on-disk dynamic fibrils (De Pontieu et al. 2007a; Hansteen et al. 2006). The maximum velocities of type I spicules are typically no higher than 40 km/s (De Pontieu et al. 2007a), and have inclinations from the vertical of 0-40° (Pereira et al. 2012).

Type II spicules have only upwards motion, meaning that they dissolve at maximum height. They reach maximum heights of about 3 Mm (quiet Sun) to 9 Mm (coronal holes). They are faster than the type Is, have smaller inclinations (between 0° and 30°), and have shorter lifetimes, between less than 1 minute to about 4 minutes. They are the most common of the two types since they seem to dominate the quiet Sun and coronal holes, while type Is are mostly found only in active regions (Pereira et al. 2012). The quiet Sun is all the area of the Sun except for the active regions where strong magnetic flux is emerging (Priest 1982). Coronal holes are regions in the corona where the magnetic field is open to interstellar space, usually located near the polar regions. They emit very little radiation, and appear darker in coronal spectral lines than that of the surrounding corona, due to lower temperatures (Schrijver and Zwaan 2008). The driving mechanism of the type II spicules is not completely clear. It has been shown from simulations that leakage of acoustic waves are highly unlikely to produce spicules with velocities higher than 50 km/s, or fading at maximum height. Reconnection of the magnetic field has therefore been considered a likely mechanism for the type II spicules (De Pontieu et al. 2007b). This remains the subject of active research.

The fastest and longest type II spicules are located in coronal holes, possibly due to the more vertical magnetic field there compared to other regions (Pereira et al. 2012). This might also be the reason why the type Is are rarely found here, since the inclination of the magnetic field influences the pressure waves ability to leak through the atmosphere (De Pontieu et al. 2007b). From simulations it is shown that oscillation periods increase with increasing inclination from the vertical of the magnetic field (Heggland et al. 2007).

Because the type II spicules fade, with no trace of down falling matter, they are speculated to be a prime source for the heat transfer to the transition region and corona (De Pontieu et al. 2007b). There has been some evidence of a coronal counterpart for type II spicules, that indicate their involvement in energy transfer into the corona (De Pontieu et al. 2009).

1.4 Dynamic fibrils

Dynamic fibrils (DFs) are jets of plasma along the magnetic field lines, found in plage regions in active regions, in the chromosphere. Figure 1.3 shows many dynamic fibrils near the center of the image. These features have also been understood better after the development of instruments and techniques making better spatial and temporal resolution attainable for observations. Such developments have made it possible to find out that most dynamic fibrils periodically move up and down in the atmosphere, with a period around 3 to 8 minutes. DFs, as well as spicules type I, are believed to originate from acoustic waves, called p-modes

(De Pontieu et al. 2007a) due to pressure being their restoring force (Priest 1982). Since these oscillations have been observed while looking at the sun as a whole, they are classified as global oscillations. The p-modes can be described by spherical harmonic functions, that makes the Sun ring like a bell struck by the plasma bubbles coming up beneath the surface of the granules (Priest 1982). These waves have a wide range of periods, with a leading period of about 5 minutes and are therefore also nicknamed "the 5-minute oscillation". P-modes originate below the solar surface, and leak into the atmosphere via the magnetic fields (De Pontieu et al. 2007a; Priest 1982). The temperature minimum in the atmosphere will filter out waves with a period longer than that of the acoustic cut-off period $P_c = \frac{1}{\nu_c} = \frac{4\pi c_s}{\gamma g}$, where ν_c is the acoustic cut-off frequency, c_s the speed of sound, γ is the specific heat ratio, and $g = g_0 \cos\theta$ the effective solar gravity with $g_0 = 274\ \mathrm{m/s^2}$ and inclination θ of the magnetic field (from the vertical). This makes p-modes with longer periods propagate along inclined magnetic fields, and p-modes with shorter periods move along more vertical magnetic fields (De Pontieu et al. 2004). The acoustic waves turn into shocks as they propagate through the atmosphere, due to the decreasing density outwards (De Pontieu et al. 2007a), which are driving the dynamic fibrils up and down.

Lifetimes of dynamic fibrils are as mentions typically around 3 to 8 minutes, where the DFs reach maximum extensions of about 1-2 Mm. They also follow parabolic non-ballistic paths in the chromosphere, with mean maximum velocities around 15-20 m/s (De Pontieu et al. 2007a). Since the duration of dynamic fibrils are known, the inclinations can be deduced from simulations. Heggland et al. (2007) found that DFs with periods of about 3-7 minutes, needed inclinations of about 0-60°.

It is only quite recently that dynamic fibrils have become a phenomenon for detailed study, and below, a detailed discussion is presented of three papers on dynamic fibrils in plage regions. These are at the basis of the work presented in this thesis:

In "High-resolution observations and modeling of dynamic fibrils" (De Pontieu et al. 2007a), a time series of about 78 minutes, obtained with the SST on the 4th of October 2005, were analyzed and compared to MHD simulations. The observations show an active region with two small sunspots. From this, 257 dynamic fibrils are investigated in H-α. To obtain narrow-band observations in the H-α line center, the Solar Optical Universal Polarimeter (SOUP) was used (for more information on SOUP see SST wiki [1] and Title and Rosenberg (1981)). The data set has a cadence of only 1 s, due to only observing one line position, the line core, and 12 exposures were used to restore 1 image with the MOMFBD technique (see section 2.1.5). It was found that the motion of the top of the DFs is accurately described by a parabola. Different properties of the DFs are obtained by fitting a parabola to

[1] $http://dubshen.astro.su.se/wiki/index.php/SOUP$

the DF path, like duration, deceleration, maximum length and maximum velocity, which will be compared to the findings of this thesis.

In "Measurements of plasma motion in dynamic fibrils" (Langangen et al. 2008b), observations of dynamic fibrils by a small pore in an active region near the disk center were investigated. From a 40 minute time series, the authors analyzed a total of 124 DFs in H-α, where 106 were used for Doppler measurements. The time series were obtained on the 23rd of September 2006, with the SST SOUP instrument. The H-α line was sampled once in the red wing and once in the blue wing, at $\pm$ 30 pm from the line core. This made for a cadence of 10.6 s, where 8.4 s was due to the alternation between these two line positions. Because alternating between the line positions spent this amount of time, it was not possible to sample more than two positions, without compromising the temporal resolution too much. From the two line positions, Dopplergrams were constructed: $D = \frac{B-R}{B+R}$, where B is the blue wing image, and R is the red wing image. They also summed the wing images to get a H-α core-like image, which were used along with the wing images to make X-T plots (see section 2.2 and section 2.3.1), and measure the DF paths. Visual inspection was used to distinguish the dynamic fibrils, and parabolas were fitted to the trajectories by finding the points of maximum change of intensity between the top of the DF structure and the background. Doppler information is extracted along these parabolas, and the maximum velocity , lifetimes and deceleration are found from the parabolic fit.

In "Spectroscopic measurements of dynamic fibrils in the Ca II λ8662 line" (Langangen et al. 2008a), spectroscopic observations of dynamic fibrils near a pore in an active region were done in the Ca II λ8862 line. The observations were obtained on May 4th 2006, and were a result of a co-observation campaign between the SST and the neighboring Dutch Open Telescope (DOT). A time series of 40 minutes were acquired, with a cadence of the order of 0.5 seconds. The TRIPPEL (TRI-Port Polarimetric Echelle-Littrow) spectograph was used at the SST, while the DOT obtained context images in the H-α continuum and line center. (More information about the TRIPPEL spectrograph can be found in the SST wiki [2] and about the DOT in Rutten et al. (2004)). TRIPPEL was used with two ports, obtaining simultaneous observations of H-α and Ca II λ8862. By using a spectrograph, full spectral profiles, at high resolution are obtained along a narrow, one dimensional line over the solar surface. Exposures were 80 ms for the TRIPPEL images, while DOT produced speckle reconstructed images at 30 s cadence. Doppler shifts are measured by fitting 4th order polynomials to the dynamic fibril signatures (diagonal line from blue to red wing) in λ-T plots (see section 2.3.1). With a linear fit to the Doppler velocities, the decelerations, maximum velocities and lifetimes for the DFs were found. The identification of the DFs has been done manually, while also comparing with traces of DFs in the DOT images.

[2] $http://dubshen.astro.su.se/wiki/index.php/TRIPPEL\_spectrograph$

Chapter 2

Methods

2.1 SST

Most of the information in this section and the sections concerning the SST specifications is found in Scharmer et al. (2003a) and the SST wiki[1].

The Swedish 1-m Solar Telescope (SST) is a ground-based refractor telescope which has a 1 meter diameter lens, and became operational in 2002. It is situated near the top of La Palma (2400 m), which is part of the Spanish Canary Islands off the north-west coast of Africa.

The SST's primary optical system consists of a lens (1.097 m diameter, 82.4 mm thick at the center) and two Zerodur mirrors (1.4 m diameter) inside the turret on top of the telescope tower (15 m). The lens acts as the vacuum window, so deformation and stress of the lens surfaces has to be accounted for. At 460 nm, the lens has a focal length of 20.3 m, which is focused through a vacuum tube down through the telescope tower, via a field mirror and a Schupmann corrector, before it leaves the vacuum tube, as seen in Figure 2.2. The vacuum tube can accomplish a vacuum of 0.2 mbar with continuously pumping, and a vacuum of 3 mbar with pumping 20 minutes 2 times a day. The latter setting is the one normally used.
The telescope has an altitude-azimuth mount (up and down, and side to side), which makes the observed images rotate, as the telescope follows the Sun's motion in the sky. The turret the lens and mirrors are mounted in, rotates to track the Sun, during observations, throughout the day.

The Schupmann corrector is a setup to correct for some of the optical aberrations. It is made up by a concave fused silica lens and a Zerodur mirror, that focus the main 1-m lens.

[1] $http://dubshen.astro.su.se/wiki/index.php/Main\_Page$

Figure 2.1: The Swedish 1-m Solar Telescope at 2400 m, within the Observatorio del Roque de los Muchachos, at La Palma. On top of the 15 m high vacuum tower, the turret with the 1-m lens tracks the Sun throughout the day. (The Mercator Telescope is seen in the background.) (*Photo: Elisabeth Jordahl*)

A field mirror (60 mm), is found at the bottom of the vacuum tube, and is a part of the Schupmann system. It will deflect the light up and off the optical axis, while still inside the vacuum tube. Between the light paths of the field mirror and the field lens, there is mounted a baffle to keep stray light to a minimum.

The tip-tilt mirror is part of the correlation tracker system that apart from stabilizing the image from seeing disturbances, also compensates for the Sun's rotation.

As seen in Fig. 1.2 and Fig. 1.3, the SST produces high spatial resolution images. High spatial and high temporal resolution can also be achieved by advanced post-focus instrumentation. The SST can observe details down to 70 km, and is one of the prime telescopes in the world for obtaining high quality solar data.

2.1.1 Seeing

The degradation of the quality of an image, due to turbulence in the Earth's atmosphere, is called seeing. The turbulence causes fluctuations of the refractive index in the path of the light (that distorts the wave-front), and is generally due to temperature differences. Bad seeing causes blurring of the image, and image motion or distortion, where the image shifts or parts of the image shifts relative to other parts. By having short exposure times, some seeing problems can be reduced by "freezing" the seeing. The exposure time is then shorter than the typical time scale of changes in the seeing (Stix 2004). Good seeing is illustrated in Fig. 2.4, and means that the atmospheric turbulence is minimal, or low enough so that the adaptive optics (see section 2.1.2) can compensate for it.

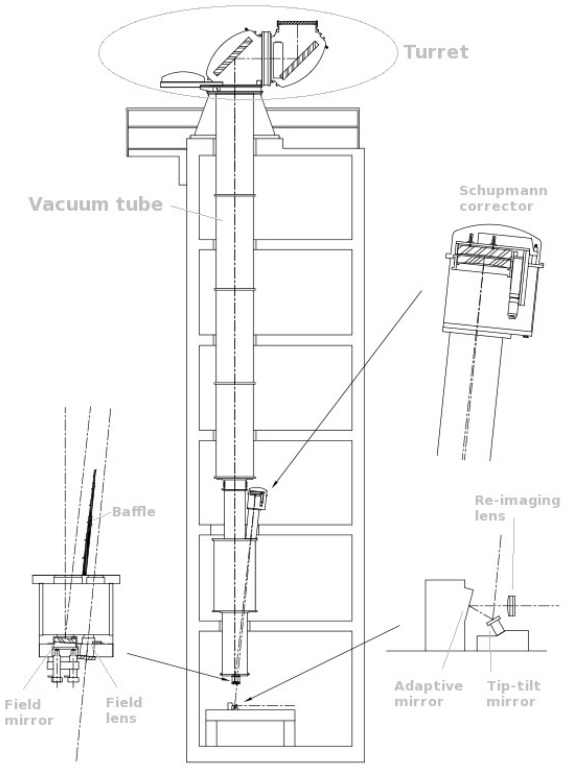

Figure 2.2: Modified SST schematic, originally from Scharmer et al. (2003a).

Seeing is a general problem in ground-based observational astronomy, but for solar observations, the Sun makes it worse, due to heating of the ground, building etc that can create local convection and turbulence (Stix 2004). The SST has a 15 m high telescope tower, that puts the main objective and light entry into the telescope above the layer that is mostly affected by convection caused by ground heating. The vacuum tube is also in place to avoid seeing inside the optical system. The evacuated air hinders the formation of thermal convection.

The top of La Plama, where the SST is located, is an ideal place for a telescope due to the conditions there. The altitude of 2400 m keeps the telescope above the lowest level of clouds (see figures 1.1 and 2.2), and decrease the amount of atmosphere the light must pass through to reach the telescope. The island also has frequent wind conditions that can make the convection from the ground minimal for a telescope that is elevated a certain distance off the ground. The wind coming in from the Atlantic Ocean is laminar, with no obstacles until it reaches La Palma, thus removing the local convection from affecting the wave-front before entering the system.

2.1.2 Adaptive Optics

Adaptive optics are systems designed to compensate for the seeing and wave-front distortion in the atmosphere. The adaptive optics (AO) used at the SST has been upgraded since 2010, but here, the setup used in June 2010 will be briefly described, and most of the information is found in the SST wiki[2] and in Scharmer et al. (2003b).

Basically, the AO consists of a deformable mirror and a wave-front sensor. The deformable mirror is together with the tip-tilt mirror and re-imaging lens the first optical elements outside the vacuum system and is mounted on the optical table, as seen in Figure 2.2. The Shack-Hartmann wave-front sensor consists of an array of 37 micro-lenses, which are hexagonal. The deformable or adaptive mirror is a bimorph mirror with 37 electrodes attached to it, see Fig. 2.3.

The tip-tilt mirror is used to compensate for tip and tilt translations (first and second order aberrations), that give rise to shifts of the whole image. In principal, the deformable mirror can compensate for this, but it has been proven to be more efficient to have a dedicated flat mirror taking care of the lowest order aberrations, and having the deformable mirror compensate for higher order aberrations. Remaining aberrations after AO corrections can in principle be compensated for by MOMFBD processing (see section 2.1.5).

A small fraction of the light is directed by a beam splitter, located just before the CRISP instrument, into the wave-front sensor system. Here the light is divided into sub-images by the lens array, and focused onto a camera. The sub-images are all the same, and are to be compared with a reference image to decide the wave-front distortion. The camera sends its images to the computer that calculates these distortions, and the changes the bimorph mirror needs, to be able to compensate for it. Karhunen-Loève (KL) polynomials are the optimal basis functions for compensating phase aberrations from seeing, so linear combinations of these are used to approximate the wave-front deformations. This information is then sent to the deformable mirror in the form of adjusted voltages that the electrodes use to deform the mirror less or more. The mirror then adapts to try to restore the original wave-front entering the Earth's atmosphere. The bimorph mirror is able to change shape 50 times per second.

2.1.3 CRISP

The information in this section is found in Scharmer (2006), de la Cruz Rodríguez (2012) and in the SST wiki.[2]

[2] $http://dubshen.astro.su.se/wiki/index.php/Main\_Page$

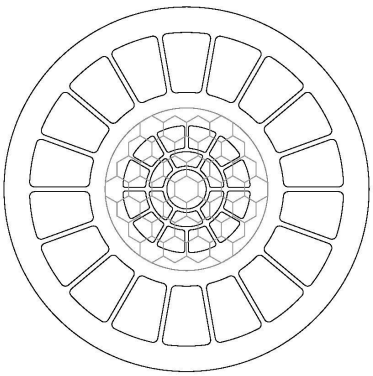

Figure 2.3: Electrode pattern of the 37-electrode bimorph mirror of the AO system. The micro-lens array is also shown in gray. Figure from Scharmer et al. (2003b)

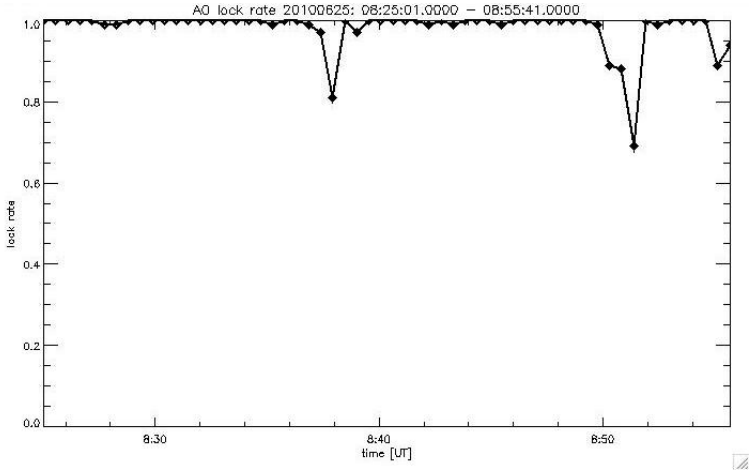

Figure 2.4: AO lock rate from the time of observing the data set under investigation. It is showing the excellent seeing conditions at the time, since the AO managed a 100% lock rate almost the entire time. The lock rate give a measurement of the seeing, and how well the AO is able to compensate for it. (Figure from the ITA La Palma wiki.)

The CRisp Imaging SpectroPolarimeter was installed at the SST in 2008. It has a wavelength range between 510 - 860 nm, which includes some important chromospheric spectral lines, like the two considered in this thesis.

As seen in Fig. 2.5, CRISP contains a number of instruments. The Chopper is a rotating wheel with an opening that synchronizes the 3 CCD cameras and sets their exposure times of 17 ms. The filter wheel selects the prefilter of the line or lines that is to be observed, and is the first step in suppressing wavelengths other than the wavelength selected. The filter wheel uses between 250 ms and 600 ms in order to change between two filters, depending on how close the filters are located on the wheel. After the filter wheel, a beam splitter directs 10% of the light to

the wideband camera, which is used for the MOMFBD restoration (see section 2.1.5). The remaining 90% of the light goes through to the liquid crystals (LC), which are used for determining the polarization properties of the light. The LCs usually change between 4 states when polarization is part of the observations. For the data set considered in this thesis, the LCs do not change state. The Fabry-Pérot interferometer (FPI) is a tunable narrow-band filter system, that allows for rapid tuning (< 50 ms). The etalons (HRE and LRE) will therefore continue the suppression of wavelengths other than the ones being observed. A polarizing beam splitter separates the light into two different polarization components (transmitted and reflected), that each goes to a respective CCD. This type of splitter along with the two cameras are used to cancel out polarization cross-talk caused by seeing. The two CCDs at the end of the light path, have 1024×1024 pixels, and operate at 35 frames per second, which gives 4 line positions per second. The data rate of CRISP is 380 gigabytes per hour.

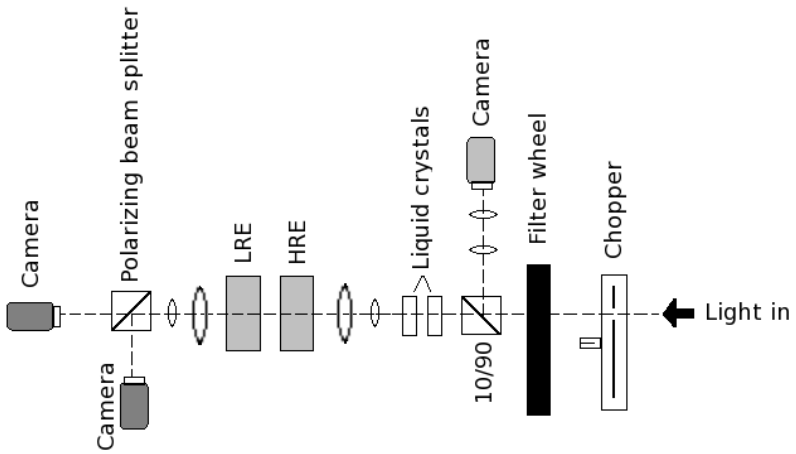

Figure 2.5: Schematic setup of CRISP instrument, which shows the path of the light.

2.1.4 Observations

The data set under investigation, is as mentioned in the introduction, a data set from observations made the 25th of June 2010. It contains a small active region (AR) that has not been numbered, located around N18, W33. The lines that have been observed, are H-α (6563 Å) in 45 line positions, and Ca 8542 (8542 Å) in 47 line positions. For more details see Table 2.1.

The diffraction limits in the table, are calculated using the Rayleigh criterion, which gives the limits in radians. Radians are converted to arcseconds by

1 rad$= \frac{360^\circ \times 60 \times 60}{2\pi}$ arcsec. The Rayleigh criterion is valid because the SST has an un-obstructed round aperture. One arcsec on the Sun is equivalent to 738 km om the surface.

SST 25/06/2010 data set			
Solar heliocentric coordinates			(x,y)=(493 $''$, 265 $''$)
Stonyhurst coordinates			N18 , W33
Observing angle θ			36° , $\mu = \cos\theta = 0.8$
Observed lines	H-α	6563 Å	45 line positions
	Ca 8542	8542 Å	47 line positions
Observing time			08:25:13 UTC - 08:55:38 UTC
Duration			00:30:25 (hours:min:sec)
Cadence of series			21.4600 s
Number of scans			86
CCD frame rate			35 frames/s
Frames per line position			8
Exposure time per frame			17 ms
FOV size			$54'' \times 54''$
Pixel size in arcsec			0$''$.0592/pixel
Diffraction limits (round aperture)	H-α		$1.22 \times \frac{\lambda_{h\alpha}}{D} \approx 0''.165$
	Ca 8542		$1.22 \times \frac{\lambda_{ca}}{D} \approx 0''.215$

Table 2.1: SST data set information.

2.1.5 MOMFBD

In this section, the information is taken from van Noort et al. (2005), Löfdahl et al. (2007) and Sekse et al. (2012).

MOMFBD is short for Multi-Object Multi-Frame Blind De-convolution, which is an image restoration technique. Image restoration is used for reducing some of the seeing effects in the observed images. For this CRISP data set, the tunable filter have sequentially sampled different line positions. Stepping through the line takes time, and means the seeing will be different for different line positions. Therefore the spectrum from a location on the Sun and will be affected by conditions in the neighbourhood. The MOMFBD can reduce this effect to some extent.

MOMFBD is based on two main assumptions, which will be discussed here. The first assumption is that during the gathering of the raw data, the solar scene does not change. This is valid because generally phenomena in the solar atmosphere change much slower than the seeing conditions in the Earth's atmosphere, which change in the order of milli-seconds. For the data set considered here, there are two strong lines sampling the solar atmosphere from the photosphere to the chromosphere.

This assumption is good for the wideband and the line wings which sample the photosphere, where the evolution time is rather long. For the chromosphere, where higher velocities are typically found, the assumption's validity should be looked into. The time it takes CRISP to do one line scan of H-α or Ca 8542, takes about 10.5 seconds. For measuring the Doppler shift in this data set, a parabola is fitted to the line core of the spectral lines. The code fits the parabola based on the values of the minimum 7 and 9 line positions of the line core of H-α and Ca 8542 respectively. The time it takes to obtain these values is 17 ms $\times$ 7 line positions = 0.952 s for the hydrogen line, and 17 ms $\times$ 9 line positions = 1.224 s for the calcium line. If a feature in the chromosphere moves with a velocity of 20 km/s (an upper value for the DFs in the 25/06/2010 data set), the time it would take to move across 2 pixels would be:

$$\frac{0\farcs0592 \times 2 \times 738 \text{ km/arcsec}}{20 \text{ km/s}} = 4.4 \text{ s}$$

So for the feature to move across 1 pixel, takes about 2.2 seconds. This implies that CRISP is sampeling the core of the two lines quickly enough to get reliable Doppler measurements.

The second assumption that the MOMFBD uses, is that the point spread function (PSF) stays constant over the image. The PSF is a measurement of how much a point source is spread out, and describes how the seeing affects the image. Since the PSF is known to change considerably over the FOV, the images are divided up into smaller overlapping sub-images. The size of the sub-images are smaller than the area where constant seeing (isoplanatic patch) can be assured. Once the MOMFBD is performed, the sub-images are put back together, resulting in a restored image of the FOV.

For this data set the MOMFBD uses 8 exposures per line position to restore 1 image, and restores the images per time step. All the individual line positions are aligned to the wideband channel, hence all line positions are aligned to each other. This reduces the effect of mixing spectral information from neightbouring locations greatly.
The amount of raw data that is gathered for just one line scan of the H-α and Ca 8542 lines, from the three cameras, are $3 \times 8 \times 45$= 1080 frames and $3 \times 8 \times 47$= 1128 frames respectively. The usable science data obtained from this, is 45 + 1 (wideband) images for H-α, and 47 + 1 (wideband) images for Ca 8542.

2.1.6 Alignment

Since the MOMFBD is applied per time step, the time series must be destretched, derotated and aligned. The Sun's rotation, although small for most SST data sets,

must also be corrected for, and the correlation tracker along with the tip-tilt will take care of that.
The raw data have a slightly larger FOV than the usable science images. Because of seeing, the position of the images can shift a little bit. These shifts are not substantial thanks to the tip-tilt mirror, that compensates largely for this effect. The remaining shifts are compensated by destretching and aligning the images. Destretching deals with seeing variations that extend more than one time step, by cross-correlating sub-fields of the images. The alignment entails calculating the cross-correlation of a big section in the images, to make sure they all end up with the exact same FOV. Hence some edges of the images must be trimmed off. Additionally, the H-α time series must be aligned to the Ca 8542 time series, due to small differences brought on by the optical system.

As mentioned before in section 2.1, the telescope has an alt-az mount. This makes the observed images rotate, due to the Earth's rotation or equivalent, the Sun's motion through the sky. This effect must of course be compensated for, and derotation is part of the alignment process.

The data set in this thesis have also been aligned with observations from the Solar Dynamics Observatory (SDO). From this alignment procedure, the exact coordinates of the SST FOV on the solar disk are found.

2.2 CRISPEX

This section is based on the information in Vissers and Rouppe van der Voort (2012) and from the CRISPEX web page[3].

The CRIsp SPectral EXplorer (CRISPEX) is an IDL application for accessing, exploring and analyzing the processed SST observations, stored as multi-dimensional data cubes. This tool was developed with the intent of having a quick and easy way to access the SST data, particularly the CRISP data. CRISPEX can handle single spectral scans, data cubes with temporal information, and data cubes with both temporal and spectral information. It can also handle data cubes with polarization information, but that has not been used for this thesis. There is also an option to have two data sets run in CRISPEX simultaneously, this way information can be extracted from the same crosscut in both data sets at the same time.

When using the program, there is a number of windows showing different information, see Fig. 2.6. Among these are a window for showing the observations, either as still pictures or as a movie running through the time frames. One window shows a λ-time plot, which is the line profile of a pixel, shown in all time frames.

[3] $http://bit.ly/crispex$

One window is showing the average line profile of the data set, with the line profile of the pixel that the cursor is currently pointing at. Another window shows the control panel with various options to manipulate the visualization of the data, while yet another shows different parameters for the data set or data sets loaded into CRISPEX. Among these parameters are the coordinates of the cursor in the image window, and the selected wavelength index of the spectral lines of the data set or data sets that is being accessed.

For this thesis, CRISPEX has been used to look at X-T (space-time) diagrams of crosscuts (see Fig. 2.6), to do an initial check for parabolas, and making save files of these crosscuts, which contain the spectral, spatial and temporal information, to be used later in the analysis procedure.

2.3 Analysis

2.3.1 IDL code

The code used to analyze the data set, was constructed based on standard IDL procedures. Figures 2.7 to 2.14 are output plots from this code made to help in the analysis of the DFs or give an indication of the results. The code restores the saved file from a certain cross-cut or slit made in CRISPEX, and extracts information from it. This saved file, gives the intensity from the slit in all of the 85 time frames, and then make a plot of what the intensity of the slit looks like temporally. This plot is called a X-T (position-time) plot. This is the first thing the code does. It reproduces and scales the X-T plot, so the parabolic shapes will be easier to recognize. The cursor is used to mark the expected start, top and end points of the DF, to fit a manual parabola. The parabola is chosen due to the work of De Pontieu et al. (2007a), who showed that the top of a dynamic fibril follows a parabolic trajectory in a X-T diagram, by analyzing observations of high temporal resolution. A better parabola is fitted, from the manual parabola, by finding the top of the DF structure, and following its position through the X-T plot. The top of the dynamic fibril stands out as a sharp change in the intensity compared to the background (see Fig. 2.7). That is why a test is put in to find the position of the steepest slope of the intensity in each time frame of the X-T plot, near the parabolic fit. This test gives the trajectory of the DFs. Both parabolas can be seen for each of the spectral lines in Fig. 2.7. The X-T plots would also give an indication of the H-α line forming higher up, due to the shift in spatial position that the DFs in H-α would show, compared to the DFs in Ca 8542.

There is also a test to check if the seeing too bad. The test will check if the maximum gradient of the intensity is located at one of the spatial endpoints in the X-T

plot's time frames. The frames with bad seeing will then be excluded from the new positions to fit the new parabola, to make the parabola more accurate.

A data cube for only the Ca 8542 core was made by finding the minimum of the line profile and saving only the information of the line position closest to the minimum. This was done to give a better visual of the dynamic fibrils in Ca 8542. Since Ca 8542 is more sensitive to Doppler shift than H-α, the line core is expected to move around much more. This might lead to more background noise in the DF trajectory in Ca 8542, making the paths more indistinguishable.

Doppler shifts

To get the Doppler shifts, a parabola is fitted to the line profile for each pixel of the X-T plot, as shown in Fig. 2.8. This is used to find the line position of the minimum. By subtracting the position of the known line core from the position of the minimum of the fitted profile, the Doppler shift of the line is found. To translate the Doppler shift according to line position into a velocity, the zero velocity must be defined. The zero velocity is defined at the line position of the fitted profile extremum of the zero velocity pixel. The zero velocity pixel is defined as the top of the DF's fitted parabola, under the assumption that the plasma is at rest at the maximum height of the DF. The line position of the zero velocity is subtracted from the minima line positions of the other pixels in the DF parabola, and multiplied with a factor containing the distance in wavelength that the shift in line positions represents. The formula is:

$$v_{DS} = \frac{\Delta\lambda}{\lambda_{core}}\, c$$

where v_{DS} is the Doppler shift velocity, $\Delta\lambda$ is the difference in wavelength, λ_{core} the wavelength of the line core, and c the speed of light.

The Doppler velocities, or line of sight (LOS) velocities are then plotted for all the pixels in all the time frames, to create a map of up flows and down flows. These Dopplergrams also feature the dynamic fibril's fitted parabolas, and show how the DFs are moving up, towards the observer (dark/black) in the beginning of the parabola, and then sink back down again (light/white), see Fig. 2.9.

Because the parabolic fit of the DF might not always precisely trace plasma at the top of the DF, investigations of the Doppler shift slightly below the top are also done. The values of the Doppler velocities are plotted against the duration of the DF, for the pixels of the fitted parabola, and at fixed pixel offsets below, as seen in Fig. 2.10. The plus signs are the actual Doppler velocities, while the linear fit of the points gives the Doppler decelerations and indicate the trend of the velocities.

To get an indication of how well the parabola fits the DF's trajectory and how far the DFs extend, the top of the DF structure is plotted along with the parabola fit.

The height or maximum extension of the DF and the duration, is shown in Fig. 2.11. The top of the DF structure is shown in plus signs, while the dashed line is the parabola fitted from these points.

Another visual aid to make sure the DF displays parabolic motion, is to step though the line, as in Fig. 2.12. The images shows, from left to right, that in the blue wing of the spectral lines the plasma is moving upwards, forming a parabola when moving closer to the line core, and finally moving back down in the red wing.

In Fig. 2.13, the λ -time plot is shown. This shows the line profiles of a selected pixel, stacked in time, which makes it is easy to see how the line profile is shifting for a DF parabola. The fitted DF parabolas for this example expands from time frame 16 to 30, and from about spatial positions 16 to 30 in H-α, and from time frame 14 to 27, and from about spatial positions 7 to 23 in Ca 8542 (see Fig. 2.7 or Fig. 2.9). So by choosing to look at a pixel in the beginning of the fitted parabola, and a pixel near the top, a diagonal line is expected to be seen at the time frames that the two parabolas extend. The diagonal line imply that the line profiles are blue-shifted at first, and become red-shifted at the end, hence the DFs are moving up and down. As expected, the shifts are greater near the start of the parabola. Due to the Ca 8542 line being much narrower than the H-α line, the shifts are much clearer in Ca 8542.

To get results comparable to previous studies, the maximum velocities, decelerations, maximum heights and durations must be acquired. Heights and durations are already found, while the proper motion velocities and decelerations are calculated by derivation of the fitted parabolas, one and two times respectively. These variables are plotted against each other, like in Fig. 2.14. For the final result, all the dynamic fibrils that have been investigated will be plotted together in a scatter plot, to see if there are any trends of their behaviour.

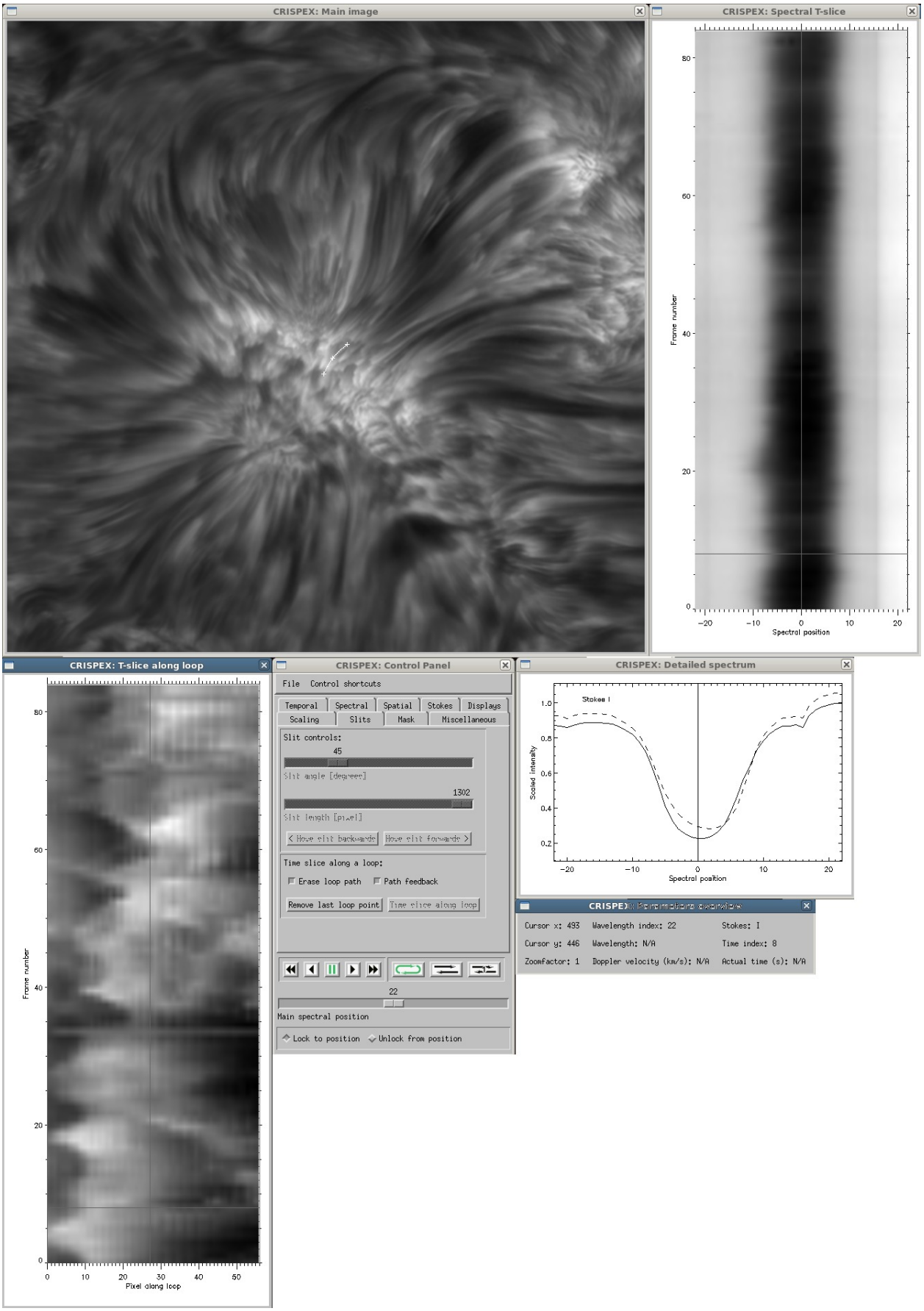

Figure 2.6: Overview of CRISPEX windows. Information in the windows, such as the X-T plot, λ-T plot, and plot of the line profile, are a result of the slit (white line) drawn in the image window.

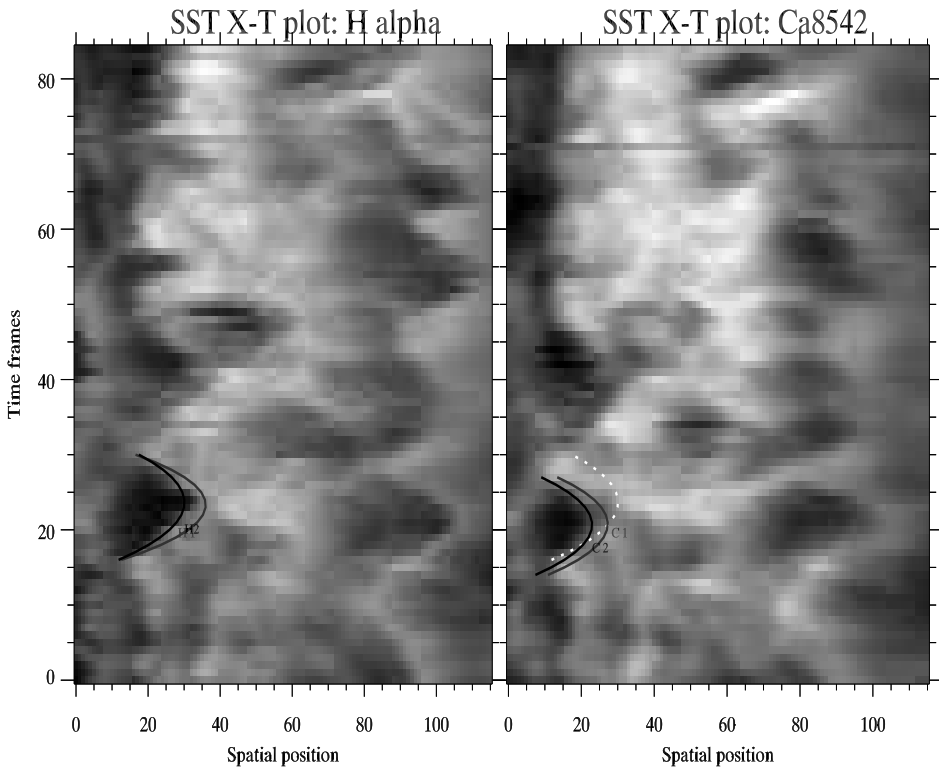

Figure 2.7: Output plots from IDL procedure: Example of X-T plot: Spatial slit made in CRISPEX, shown for all time frames. Here the parabolic motion, that the DFs display, can be seen clearly. The parabolas are generally much sharper in H-α, than in Ca 8542. C1 and H1 (gray) are the first manual parabolas in Ca 8542 and H-α respectively. The other parabolas (C2 and H2 in black), is the fitted parabolas used for collecting data. (In the Ca 8542 plot, the white dotted parabola is the fitted H-α parabola, meant to indicate which dynamic fibril is under investigation.)

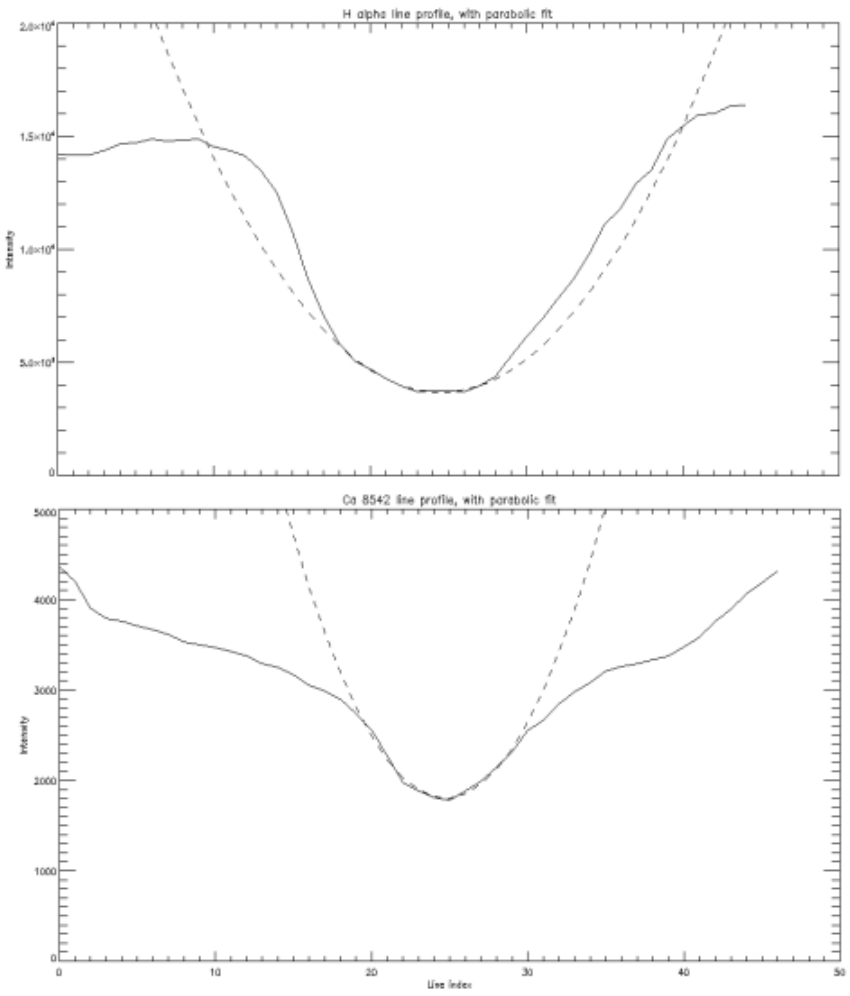

Figure 2.8: Output plots from IDL procedure: Parabolas fitted to the core of the profiles for the two spectral lines. This is done for all the pixels in the X-T plots.

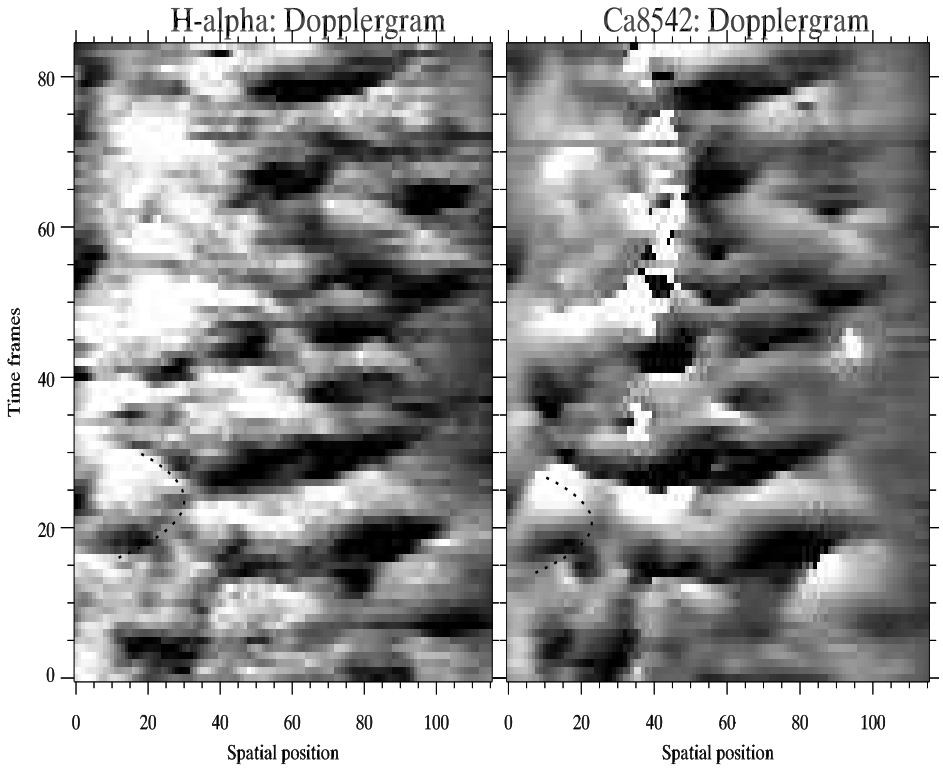

Figure 2.9: Output plots from IDL procedure: Doppler-time plot of the two spectral lines, with their respective fitted parabolas. The Doppler velocities are defined to be zero at the top of the fitted parabolas. The images are scaled between -3 and 5 km/s for H-α, and between -5 and 6 km/s for Ca 8542.

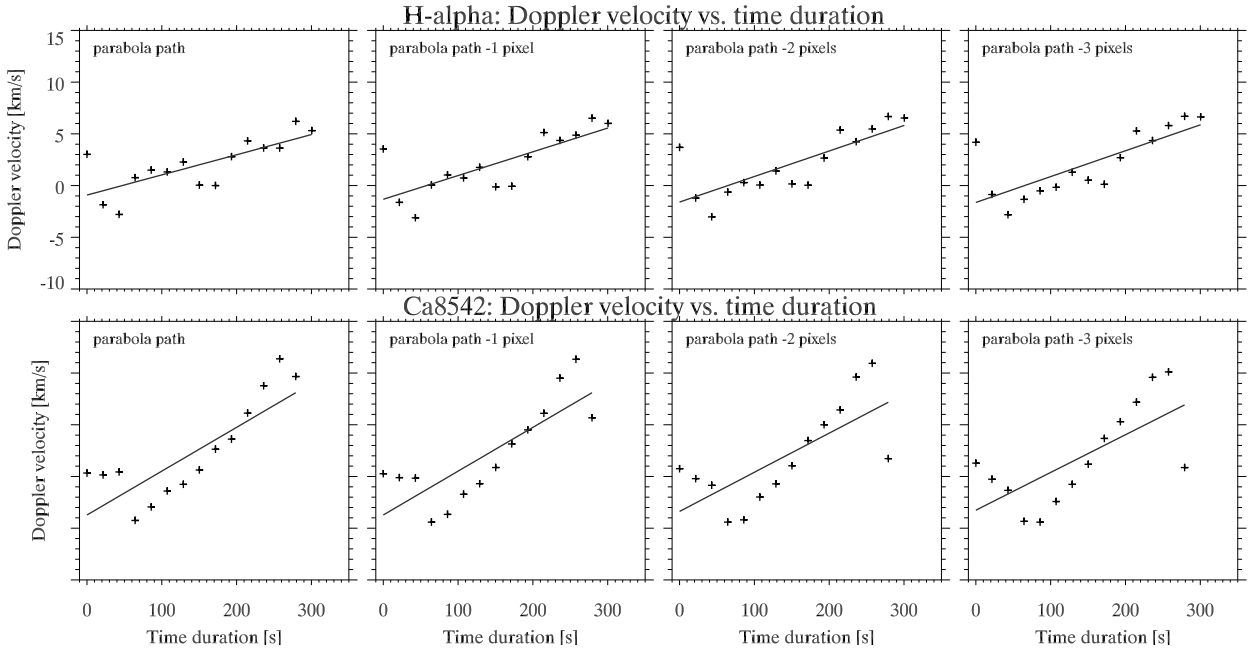

Figure 2.10: Output plots from IDL procedure: The Doppler velocities against time duration of the dynamic fibril in H-α (top row) and Ca 8542 (bottom row) through the fitted parabolas, as well as for the shift of the parabolas one, two and three pixels lower. The actual Doppler velocities (+) are linearly fitted with a line to show the trend and estimate the Doppler decelerations.

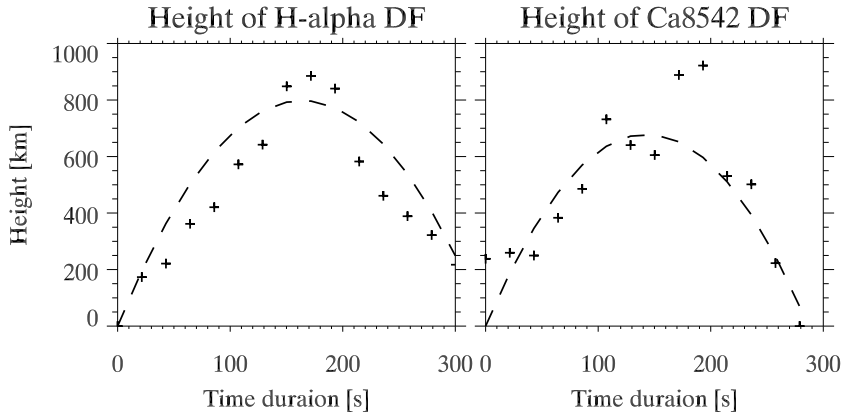

Figure 2.11: Output plots from IDL procedure: The maximum extension or height and duration of the dynamic fibril in H-α, and Ca 8542. The plus signs mark the top of the DF found for each time step from the location of the maximum intensity gradient. The dashed line marks the fitted parabola.

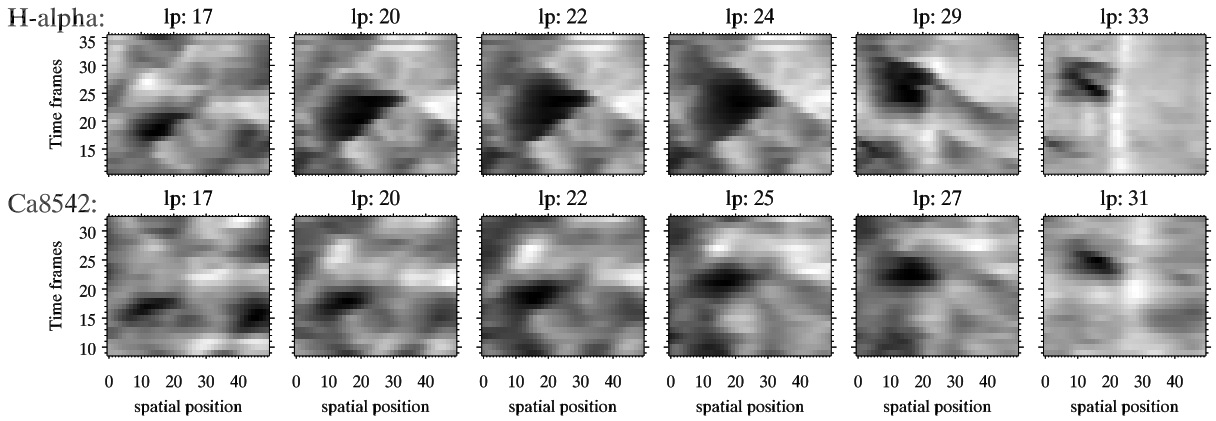

Figure 2.12: Output plots from IDL procedure: Stepping through the lines of a dynamic fibril in H-α and Ca 8542, which is just looking at selected line indexes in the blue wings, near the cores, and in the red wings. Line core of H-α and Ca 8542 are line position 22 and 23 respectively.

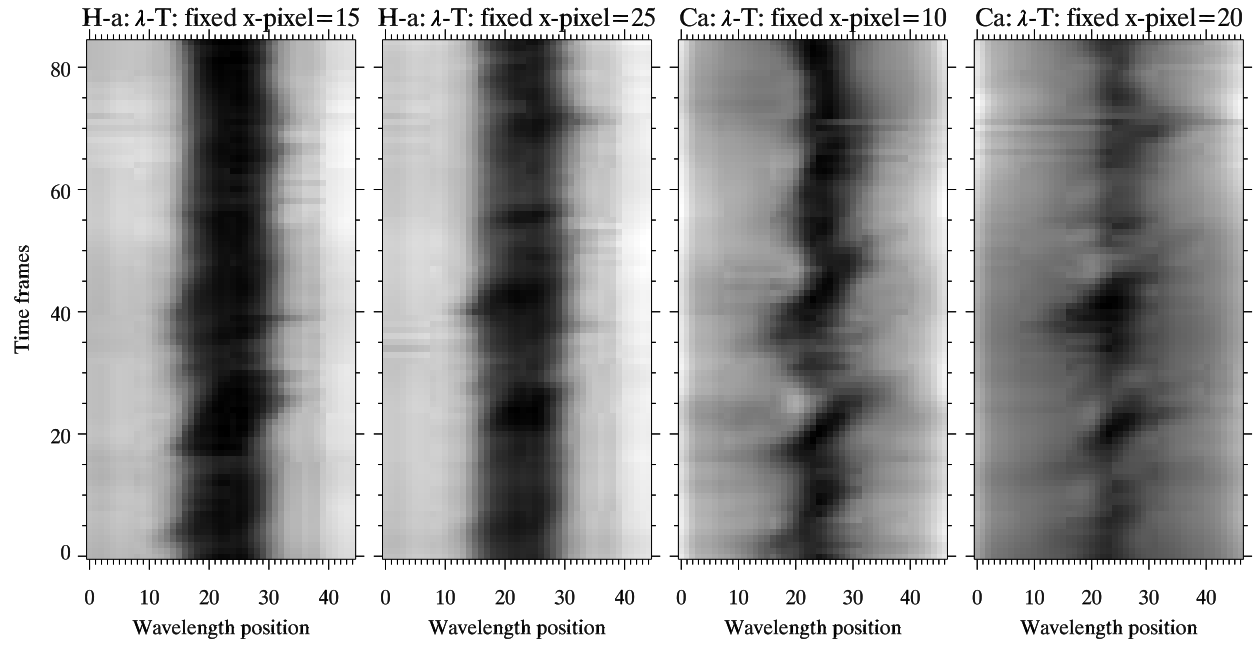

Figure 2.13: Output plots from IDL procedure: λ-time plot of selected pixels at the base of the DF and near the top, in both H-α and Ca 8542. The image shows shift in the line profiles of the spectral lines for a given pixel, throughout the time series. The DF under investigation expands a parabola from time frame 16 to 29 in H-α, and 16 to 28 in Ca 8542. The DF can be traced longer near the base of the DF, than near the top. The Ca 8542 plots clearly show the traces of multiple DFs at this location.

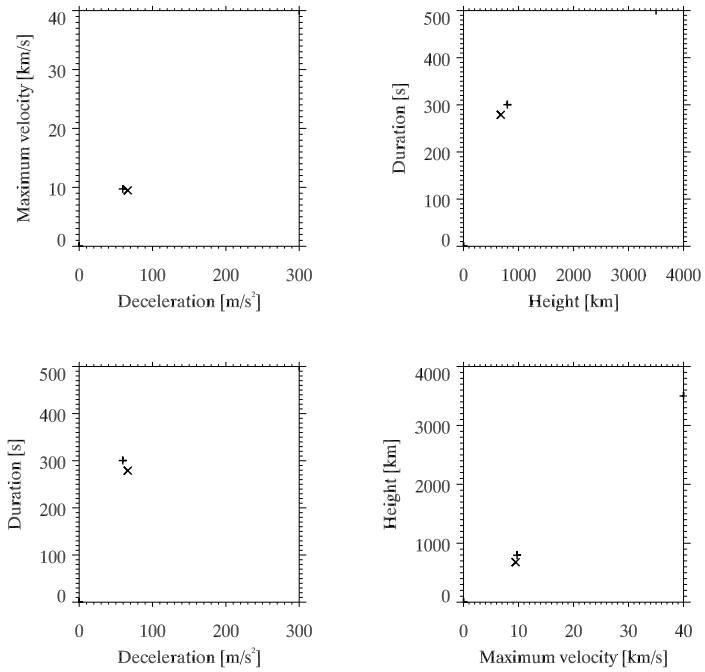

Figure 2.14: Output plots from IDL procedure: Height (km) , duration (s), maximum velocity (km/s) and deceleration (m/s^2) derived from the fitted parabolas in H-α (+) and Ca 8542 (x). (Results for only one dynamic fibril.) The measurements are shown in a 4-panel scatter plot format for direct comparison with the corresponding scatter plots of De Pontieu et al. (2007a).

Chapter 3

Results

3.1 Observed parameters

A total of 63 DFs were considered for analysis, following the methods described in section 2.3.1, of which 50 where measured in detail. Due to "bad" results, some DFs were not taken into account. In some cases the DF's manually fitted parabola would not always follow the visible path of the DF, yielding results for something other than the DF. In other cases, the results were only obtainable for the hydrogen line and not for calcium, so these events were considered unsuitable for this study. Both these cases indicate that the code used in this thesis was not optimal for all the DFs that could have been investigated.
The 50 dynamic fibrils that have been investigated, have been taken from the slits drawn in CRISPEX. Figure 3.1 shows the location of these slits, drawn on a H-α core image. In some of these slits, several DFs have been prominent within one slit.

In Fig. 3.2 and Fig. 3.3 the height or maximum extension of the top of the DF, found from the automated method, is plotted against duration for all dynamic fibrils in H-α and Ca 8542 respectively. The figures show the measured top of the dynamic fibril marked with plus signs, and the fitted parabola as a dashed line. The assumption of a parabolic trajectory for the top of DFs, is shown to be a good assumption in these figures. H-α often show a good fit, while there is more variation in Ca 8542. Each DF is numbered (top right corner in each plot), so that the same number refers to the same dynamic fibril. This is also the case for Fig. 3.4 and Fig. 3.5, where the Doppler velocities against the duration are shown. The Doppler information in these two latter figures, is from one pixel shifted down from the pixels of the parabola path fitted to the top of the DFs. This is to guarantee that the information is taken inside the DF's path. The figures show clear indication of

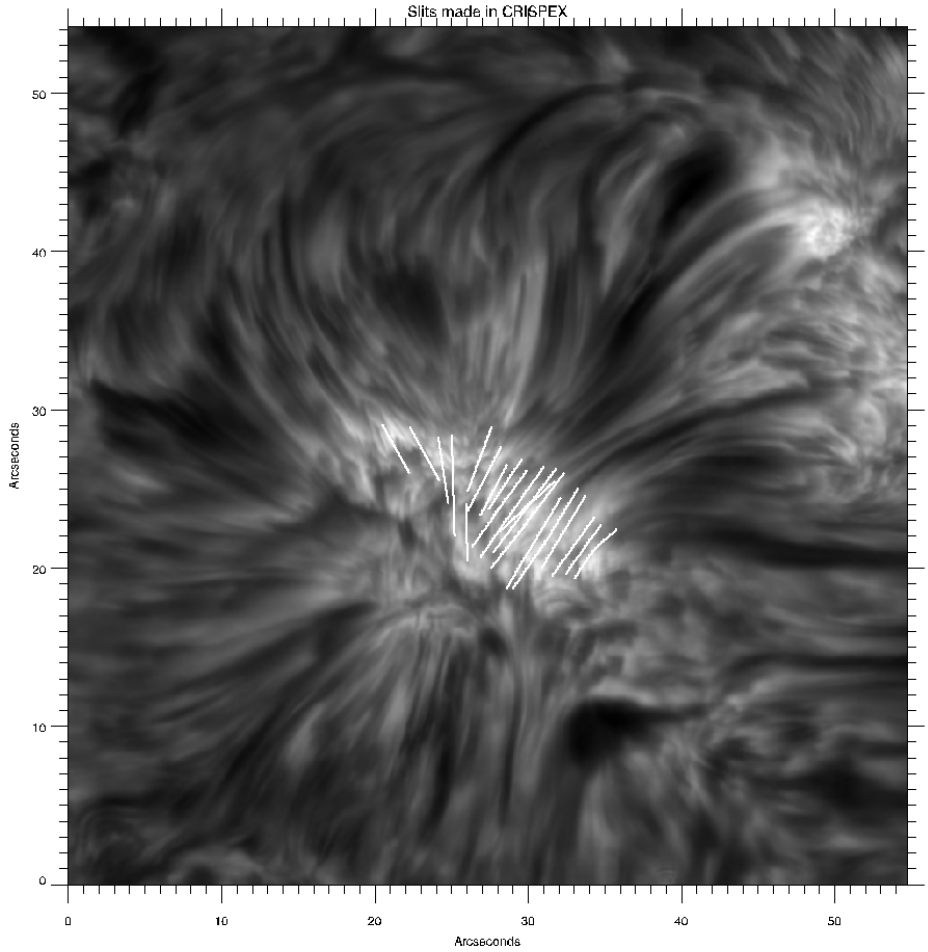

Figure 3.1: H-α image with all the slits drawn in white lines, containing the dynamic fibrils that has been analyzed.

movement from blue-shift to red-shift, as is expected from the up and down motion of the dynamic fibrils. Plus signs show Doppler velocities, while a linear fit indicates the trend. The Doppler decelerations are calculated from this linear fit.

In Table 3.1, the mean properties of the dynamic fibrils are listed, along with the sample standard deviation. The lifetimes have a mean of 230 s and 217 s ($\lesssim$ 4 min) for H-α and Ca 8542 respectively, while ranging from 129 s ($\approx$ 2 min) to 343 s ($\approx$ 6 min) for both lines. The fact that the two lines have identical time range is due to the low temporal resolution.
For the lengths of the DFs, their mean heights were 808 km for H-α and 698 km for Ca 8542. H-α DFs have a range of 210 to 1662 km, while DFs in Ca 8542 have a range of 114 to 1481 km.
The maximum velocities obtained from the fitted parabolas, show mean maximum velocities not so dissimilar in the two spectral lines, ranging between 5.6 and 24.2

Statistical properties of the 50 measured dynamic fibrils		
Parameter	H-α value	Ca 8542 value
Lifetimes (s)	230 ± 55	217 ± 54
Heights (km)	808 ± 331	698 ± 330
Maximum velocities (km/s)	13.4 ± 4.6	12.2 ± 5.3
Decelerations (m/s^2)	117 ± 52	112 ± 61
Maximum Doppler velocities (abs) (km/s)	4.5 ± 1.9	6.0 ± 3.0
Doppler decelerations (m/s^2)	27.5 ± 12.8	29.2 ± 17.1

Table 3.1: Statistical properties of the 50 dynamic fibrils that have been analyzed in this thesis. The mean values are shown, along with the standard deviation.

km/s for H-α, and from 1.8 to 24.8 km/s for Ca 8542.
Decelerations also have quite similar values, 117 m/s^2 and 112 m/s^2 for H-α and Ca 8542 respectively. Decelerations range between 42 and 243 m/s^2 for H-α, and between 14 and 295 m/s^2 for Ca 8542.
The maximum Doppler velocities with means of 4.5 km/s and 6.0 km/s for H-α and Ca 8542, range from 1.4 to 10.0 km/s in H-α, and from 1.2 to 15.4 km/s in Ca 8542. The Doppler decelerations are found from the linear fit of the Doppler velocities shown in Fig. 3.4 and Fig. 3.5. They have a range of 5.4 to 57.6 m/s^2 in H-α, and of 1.2 to 76.6 m/s^2 in Ca 8542.

From the scatter plots in Fig. 3.6, there seems to be a clear positive linear correlation between maximum velocity and deceleration (top left), duration and height (top right), and height and maximum velocity (bottom right). The duration vs. deceleration plot (bottom left) does not seem to show an as clear (negative) correlation. By fitting a linear line to the scatter points in all the plots, of H-α and Ca 8542 respectively, clear correlation is found for all plots, except for the duration vs. deceleration plot, which shows a weaker correlation in Ca 8542. When calculating the linear Pearson correlation with the standard IDL function CORRELATE, values of the correlation between -1 and 1 are found for these plots. For the maximum velocity vs. deceleration plot a correlation value of 0.84 is found for the H-α line, and 0.89 for the Ca 8542 line. For the duration vs. height plot, correlation values of 0.58 and 0.53 are found for H-α and Ca 8542 respectively. In the duration vs. deceleration plot, values of -0.52 and -0.39 were found for H-α and Ca 8542. Lastly, correlation values for the height vs. maximum velocity plot were found to be 0.78 for H-α and 0.84 for Ca 8542. Plots containing the duration, seem to make small jumps in time that makes the data points line up horizontally. This is caused by the low temporal resolution, and can only be improved by decreasing the cadence of the observations.

The scatter plot of the maximum Doppler velocity vs Doppler deceleration in Fig. 3.7, seem to be showing some correlation. With a linear fit of the points, it becomes clear that Ca 8542 shows a clear correlation, while H-α shows a weaker correlation.

Calculation the actual values, yield correlation values of 0.32 for H-α and 0.56 for Ca 8542.

Figure 3.8 shows a scatter plot of the maximum velocities and decelerations for the proper motion measurements as well as the Doppler measurement. The proper motion values are shown in red plus signs and blue x-signs for H-α and Ca 8542 respectively, and in red diamonds and blue triangles for the Doppler values. The Doppler measurements seem to extend the correlation of the proper motion measurements down to smaller values.

By comparing the obtained H-α data points for maximum velocity vs. deceleration from this thesis, with the data points of De Pontieu et al. (2007a), Fig. 3.9 is produced, where the data of the article are shown in black (x), and the thesis data is shown in red (+). The data obtained in this thesis seem to coincide nicely with the data from the article.

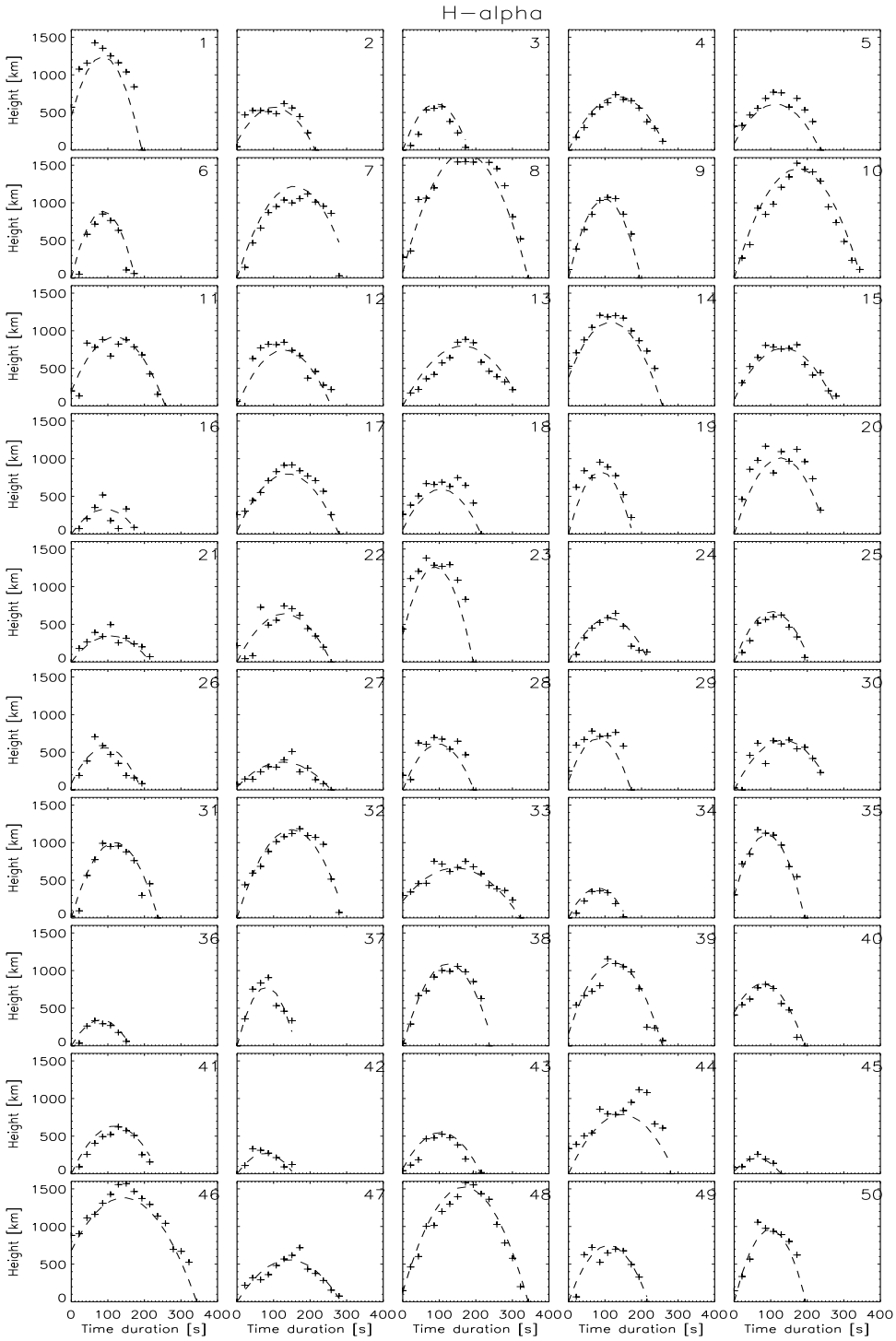

Figure 3.2: Height vs. time for all dynamic fibrils in H-α, numbered 1 to 50 in the right corner of each DF. The plus signs show the location of the top of the dynamic fibril's structure measured from the maximum intensity gradient, while the dashed line shows the parabola fitted to the top of the DF's structure.

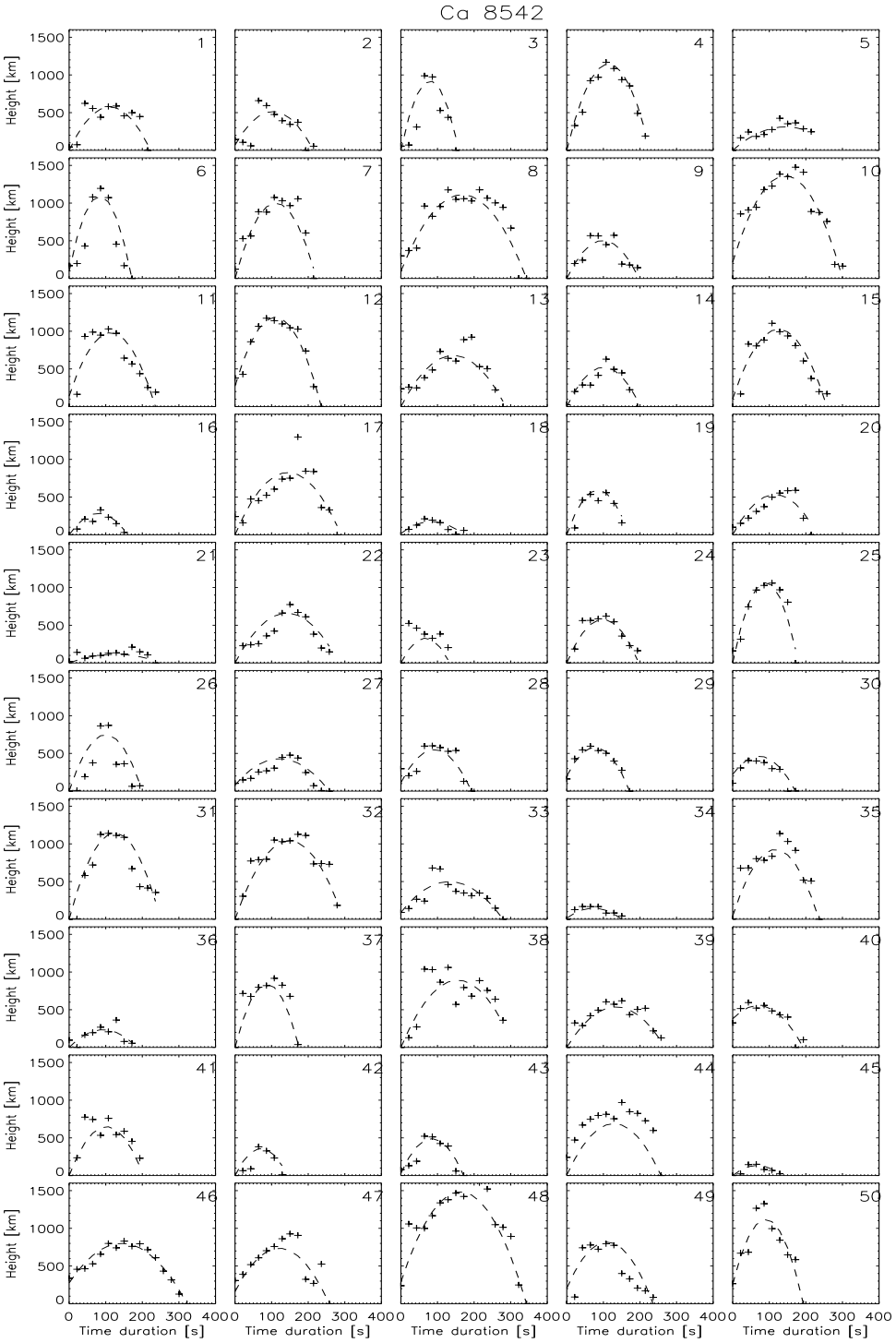

Figure 3.3: Height vs. time for all dynamic fibrils in Ca 8542, numbered 1 to 50 in the right corner of each DF. The plus signs show the location of the top of the dynamic fibril's structure measured from the maximum intensity gradient, while the dashed line shows the parabola fitted to the top of the DF's structure.

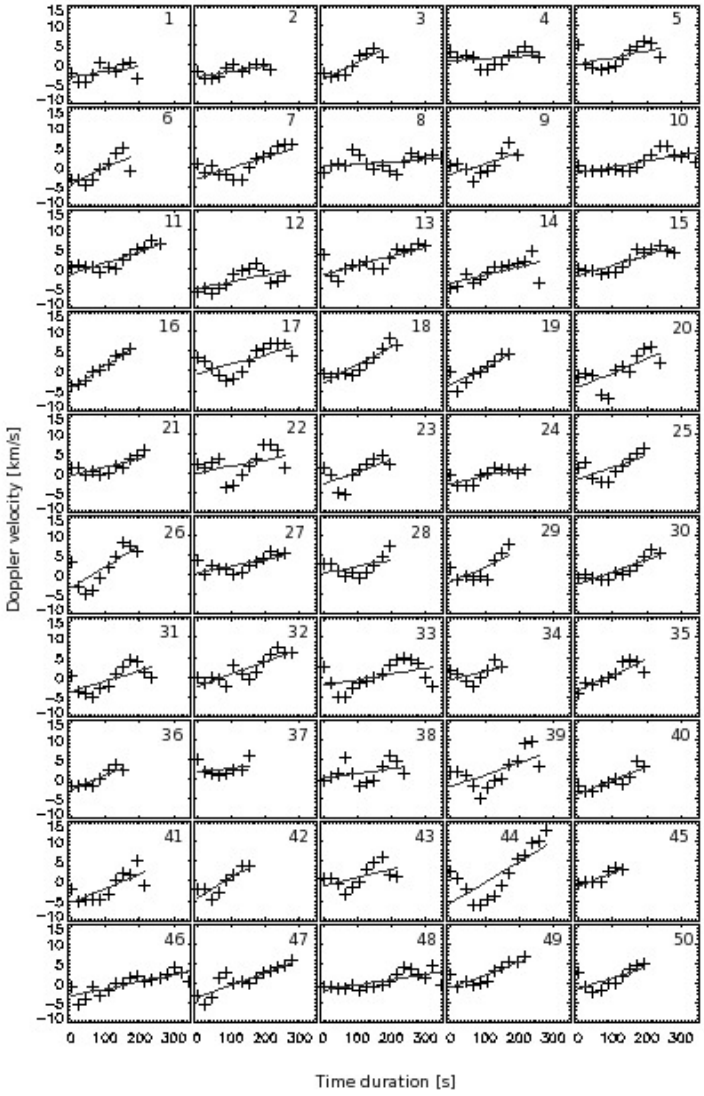

Figure 3.4: Doppler velocity vs. duration for all dynamic fibrils in H-α, shown for one pixel lower than the fitted parabola of the DFs. The x-axis shows velocities from -10 km/s to 15 km/s, and the y-axis shows the duration from 0 s to 350 s. The plus signs show the Doppler velocities , with a linear fit (solid line).

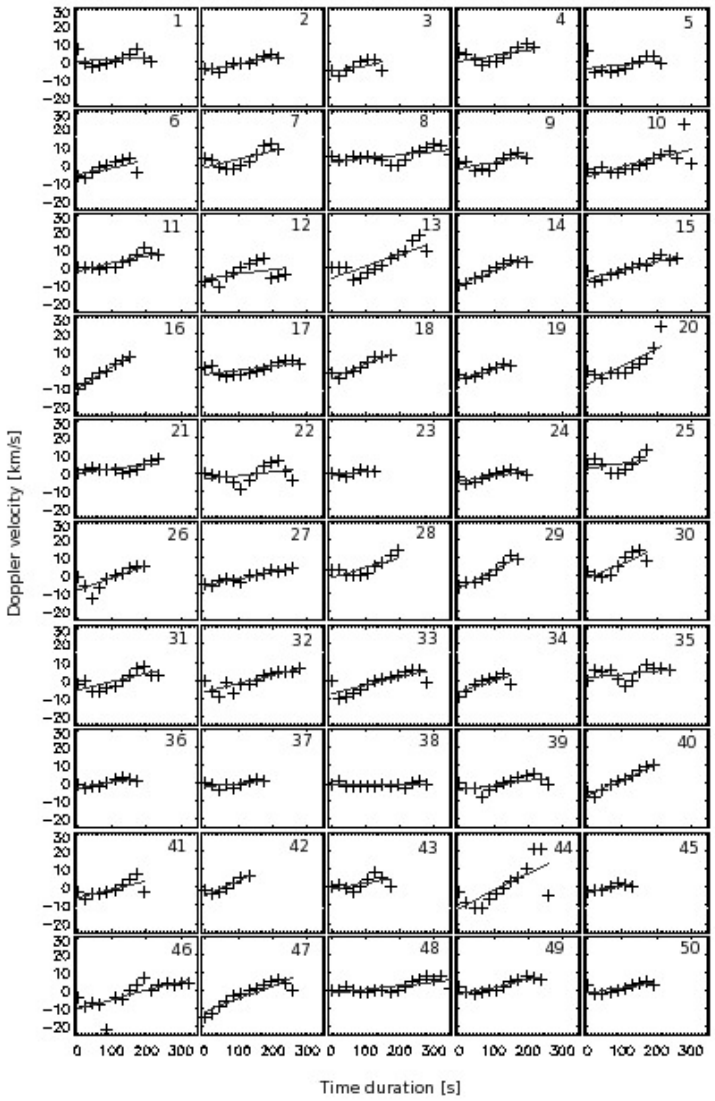

Figure 3.5: Doppler velocity vs. duration for all dynamic fibrils in Ca 8542, shown for one pixel lower than the fitted parabola of the DFs. The x-axis shows velocities from -15 km/s to 20 km/s, and the y-axis shows the duration from 0 s to 350 s. The plus signs show the Doppler velocities , with a linear fit (solid line).

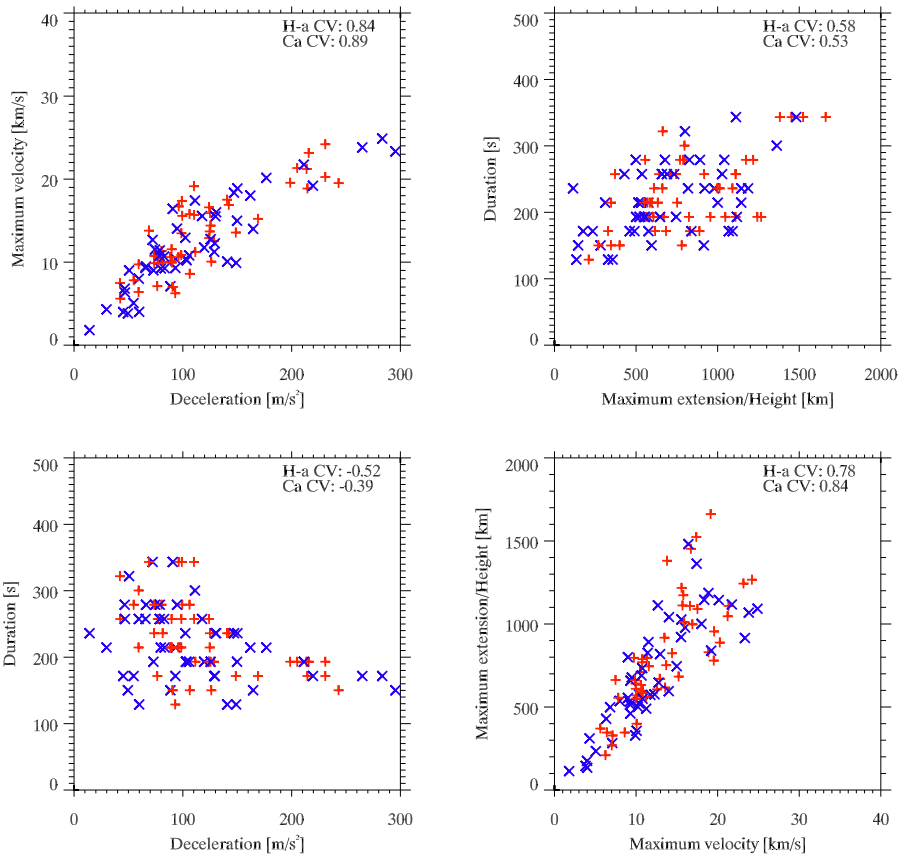

Figure 3.6: Scatter plots with parameters from all the dynamic fibrils that were investigated, in H-α (red plus signs) and Ca 8542 (blue x-signs). Top left: maximum velocity vs. deceleration. Top right: duration vs. height. Bottom left: duration vs. deceleration. Bottom right: height vs. maximum velocity. Values in the top right corner of all the plots are the correlation values (CV) for H-α and Ca 8542. For the plots containing the duration, the data points seem to line up horizontally. This is caused by the low temporal resolution.

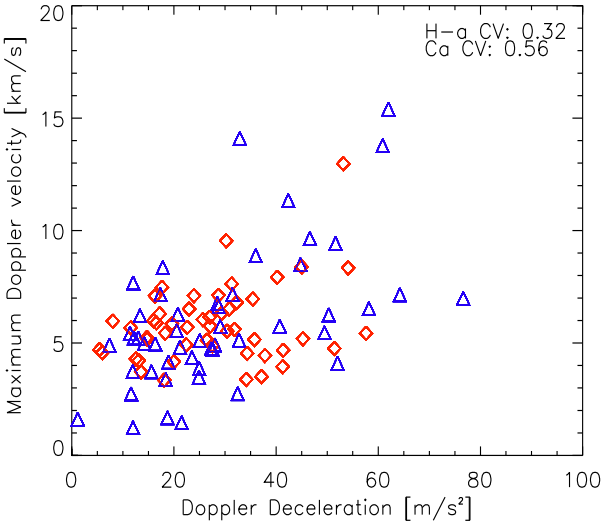

Figure 3.7: Scatter plot of maximum Doppler velocity vs. Doppler deceleration of all 50 dynamic fibrils, in H-α (red diamonds signs) and Ca 8542 (blue triangles). Values in the top right corner of the plot are the correlation values (CV) for H-α and Ca 8542.

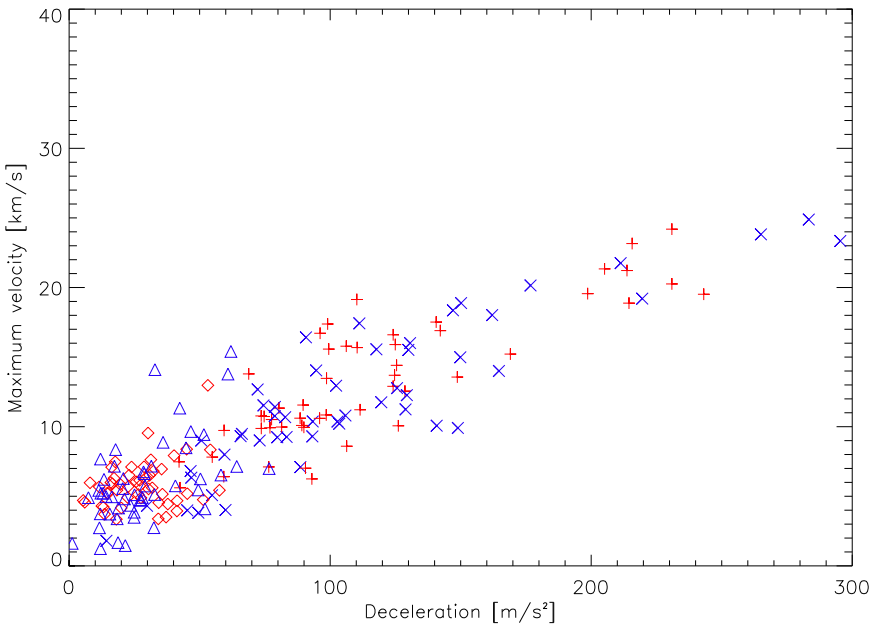

Figure 3.8: Scatter plot of maximum velocity vs. deceleration of all 50 dynamic fibrils, with both proper motion values and Doppler values. Proper motion values in H-α are shown in red plus signs and in blue x-signs for Ca 8542, while Doppler values are shown in red diamonds for H-α, and in blue triangles for Ca 8542.

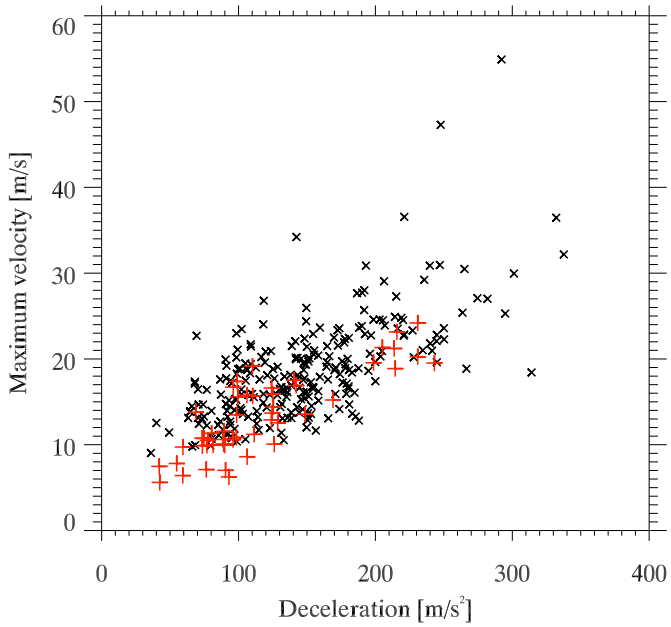

Figure 3.9: H-α data from De Pontieu et al. (2007a) in black (x) and H-α data from the SST 25/06/2010 data set in red (+).

Chapter 4

Discussion and conclusion

4.1 Discussion

The 50 dynamic fibrils investigated have mainly been found near the center of the FOV, as seen in Fig. 3.1. This is were we find the small pores and densest concentration of magnetic bright points. Playing through the time series in CRISPEX, a lot of dynamic fibrils were seen near these bright points. The region just below the center seemed more static due to the lack of moving features, but by inspecting the λ-time diagrams, many DFs were indicated, with seemingly large Doppler shifts. The lack of visible up and down motion, in this area, might be explained by the line of sight being parallel to the DFs there, instead of perpendicular. Indeed, the slits were mainly drawn roughly along the limb direction, which is towards the upper right in Fig. 3.1.

Owing to a time consuming selection process, trying to find slits in CRISPEX that yield usable results in both H-α and Ca 8542 with the IDL code, 50 DFs seemed like a viable sample of this data set.

By fitting the line profile with a parabola in the code, which usually has resulted in a very good fit, more accurate data might have been achieved by fitting a Gaussian curve or a Voigt profile. One of these curves might have been better for at least one of the lines, since their line profiles are so different. The fit of the DF trajectory with a parabola, might also have yielded more precise results, if the search interval of the steepest slope-test was confined more than in this code. But then there should also have been a more accurate preliminary parabola, than the one obtained by visual inspection, since this depends on the subjective opinion of the person that is manually investigating the DF. For some DFs the manual three-point clicking procedure to get the initial parabola fit had to be done more than once, due to an ill-fitting parabola. If these DFs had not been redone, some of their values would

have been completely off. For instance, the height would have been either too low compared to the X-T plots, or too high, and the Doppler velocities would not be connected to the rise and fall of the DFs.

For the Doppler-time plots, the zero Doppler velocity was defined by the line profile's minimum for the pixel at the top of the fitted parabola. An alternative way to do this would have been to take the average of the line profile shifts of the entire FOV and defined the average as the zero Doppler velocity. This is however not expected to differ much from the method that has been used, due to the high Doppler shift obtained.

The H-α DFs seem to fit the parabolas better than for the Ca 8542 DFs in Fig. **??** and Fig. **??**. It was harder to identify the dynamic fibrils in the Ca 8542 line, than in the H-α line. The H-α DFs were generally much clearer and had better defined parabola paths, than the corresponding Ca 8542 DFs, which were often more diffuse. The reason for this might be that the Ca 8542 line is formed lower than the H-α line, and that the temperature increase in the transition region ionizes the hydrogen, giving this line a cleaner cut-off of the formation height. **?** speculate about the possibilities of heating taking place at the top of the H-α DFs, due to H-α forming in layers up to the transition region boundary. To find out if the transition region boundary is just on top of the H-α formation height, is something that could potentially be observed with the SDO transition region diagnostic He II 304 Å line, and something to investigate in the future. Another reason for the diffuse Ca 8542 DF trajectory, might be that the Ca 8542 line is more sensitive to background noise due to shifts in the line minimum intensity, than the H-α line. To get clearer DF paths in the Ca 8542 line, the cadence of the images should be smaller.

From figures 3.2 and 3.3, it seems like the DFs extend a similar number of time frames in both lines. By calculating the difference in time frames a certain DF extends in H-α and in Ca 8542, it was found that 36$\%$ of the DFs extended the same number of time frames in both H-α and Ca 8542, while 42$\%$ of the DFs have only a difference of one time step, which corresponds to a duration difference of 21.46 seconds. But, this similarity may also be caused by wrongly determining the start or end of the manually fitted DF parabola.
Additionally, from the figures, it looks like the DFs in H-α are generally a bit higher than in Ca 8542. This is also pointed out by Table 3.1. By going through the maximum extension or height (from the DF's base-point to the highest point) of the fitted parabolas, it was found that 64 $\%$ of the fitted parabolas were higher in H-α than in Ca 8542. This could be related to the Ca 8542 trajectories being more diffuse, and the fact that the DFs fitted parabola is only fitted to the visual line core information. From the IDL code output of stepping through the line, it was sometimes seen that the Ca 8542 line would start at an earlier spatial position than what was shown in the line core. This indicates that the lifetimes and heights might be larger for Ca 8542 than what was measured here.

To be sure that the fitted parabolas in figures 3.2 and 3.3 were actually tracing out DFs, Dopplergrams and λ-T plots gave additional confirmation, by indicating up and down flows in the parabola path. The parabola that fitted the DFs in the X-T plots, would usually fit nicely in the Dopplergrams as well. Within the Dopplergram parabola there would be a darker half that turned into a brighter half as time evolved, indicating blue-shift (up-flow) and red-shift (down-flow) respectively. For the λ-T plots, the DFs would turn up much clearer in Ca 8542 than in H-α (see Fig. 2.13), this is due to calcium having a more narrow line profile than H-α, which makes it more sensitive to Doppler shifts. Usually these λ-T plots would show indications of more up and down motion at later times as well, something that also would be visible in the X-T plots.

From Fig. 3.4 and Fig. 3.5, it seems that H-α and Ca 8542 have very similar Doppler velocities, and hence not very different Doppler deceleration. This is also underlined in Table 3.1. Statistically half the DFs have their maximum (absolute) Doppler velocity measured in calcium. For the Doppler decelerations, the Ca 8542 line seem to have a larger spread of values, which is also clear from Fig. 3.7, where the Ca 8542 values are shown in blue triangles, and H-α values in red diamonds. The H-α values are more confined to the lower left corner compared to the Ca 8542 values.

From Table 3.1 the differences between the dynamic fibrils in H-α and Ca 8542 can be seen. From this table it is clear that the DFs do not have much longer lifetimes in H-α, compared to Ca 8542. The mean maximum velocities are also not so different, but the H-α heights are generally larger. The decelerations are also higher in H-α than in Ca 8542, although not by much, and are clearly lower than the solar gravity of 274 $\mathrm{m/s^2}$ for both lines. This is strengthening the argument that DFs follow non-ballistic parabolic paths and are not driven by gravity.

For the maximum Doppler velocities, the means in H-α and Ca 8542 are not that different, but the range in Ca 8542 is larger. The same applies to the Doppler decelerations. The values are not very large, but this may be caused by the DFs selection process. Selecting DFs based on visual up and down motion of the DFs, imply that the DFs have a near perpendicular angle to the line of sight, and therefore have lower Doppler velocities than DFs that are parallel to the line of sight.
There are large differences in the values of proper motion maximum velocities and decelerations, and the corresponding Doppler measurements. Apart form a possible bias through the selection process here as well, another reason might be that the Doppler measurements are influenced by the atmospheric conditions over the height that the spectral lines form.

If previous studies are correct saying DFs with lifetimes longer than 3 minutes tend to have more inclined magnetic fields, the magnetic field along these dynamic fibrils has to be inclined somewhat, since the mean duration is about 4 minutes.

Since this data set lacks Stokes data, this is hard to confirm, but might be possible to investigate further with new observations.

From Fig. 3.6, there are strong indications of linear correlations between maximum velocity and deceleration, lifetime and height, and height and maximum velocity, as mentioned before. Numerical simulations have shown that these correlations are signs of a shock wave driving mechanism (Hansteen et al. 2006; De Pontieu et al. 2007a; Heggland et al. 2007), and correlation of the plots coincide with results of previous studies.

For the maximum Doppler velocity and Doppler deceleration plot in Fig. 3.7, the correlation in Ca 8542 is clear. In H-α the correlation is weaker, but this might be due to the broadening of the H-α line, making it less sensitive to Doppler shifts than the Ca 8542 line is.

Figure 3.8 shows the proper motion measurements combined with the Doppler measurements of maximum velocity and deceleration. The Doppler values seem to fit in nicely with the proper motion values.

De Pontieu et al. (2007a)

The parameters of the 257 DFs analyzed in this paper are listed in Table 4.1 as means with the standard deviation, as well as the stated range of the values. Comparing this table with the properties of the H-α DFs in the data set of this thesis, it is clear that the De Pontieu et al. (2007a) values are generally higher. This might be caused by intrinsic differences between the two observed active regions. Note that the active region of this thesis is smaller than the one observed in De Pontieu et al. (2007a). For the lifetimes, the range of values for H-α data from the thesis, are within the range found in this paper. The same is the case for decelerations. Due to the 1 second cadence of the De Pontieu et al. (2007a) data set, DFs are expected to be much clearer and sharply defined here, than in the data set of the thesis, which has a cadence of 21.46 seconds.

Properties of the 257 H-α dynamic fibrils in De Pontieu et al. (2007a)		
Parameter	Mean	Range
Lifetimes (s)	290 ± 85	120 - 650
Heights (km)	1250 ± 620	400 - 5200
Maximum velocities (km/s)	18 ± 6	8 - 35
Decelerations (m/s^2)	146 ± 56	40 - 320

Table 4.1: Properties of the dynamic fibrils that have been analyzed in De Pontieu et al. (2007a).

The data in De Pontieu et al. (2007a) are not corrected for projection effects, and neither are the data used in this thesis. In the paper, the authors try to extrapolate the direction of the magnetic field to find the projection effects of the DFs, but find that this gives possibilities of significant errors. If there had been magnetograms with high enough resolution, finding the inclinations of the magnetic field might have made the estimation of the projection effects possible.

From Fig. 3.9, the observed H-α data from the thesis corresponds well with what was found in De Pontieu et al. (2007a). This strengthens the argument for DFs having acoustic shock as their driving mechanism.

Langangen et al. (2008b)

The properties of the 124 H-α DFs investigated in this paper are listed in Table 4.2, as means with corresponding standard deviations. The Doppler velocities and decelerations are based on 106 DFs. By comparing obtained H-α properties from the thesis with the values in Langangen et al. (2008b), values from the thesis are still a bit on the small side, although this difference is not as big as with the De Pontieu et al. (2007a) paper.

Properties of the 124 H-α dynamic fibrils in Langangen et al. (2008b)	
Parameter	Mean
Lifetimes (min)	258 ± 56
Maximum velocities (km/s)	18.6 ± 6.6
Decelerations (m/s^2)	142 ± 64
Doppler velocities (km/s)	6.4 ± 2.1
Doppler decelerations (m/s)	33.7 ± 15.6

Table 4.2: Properties of the dynamic fibrils that have been analyzed in Langangen et al. (2008b). The mean values are shown, along with the standard deviation.

By only regarding the points in Fig. 3.8 for the H-α line (red points), it is found that this plot is similar to the scatter plot found in the Langangen et al. (2008b) paper. There the Doppler measurements are also confined mostly to the lower left corner of the plot, and proper motion measurements are spread diagonally from the this corner and up. The difference is that in Fig. 3.8, there is less overlap between the Doppler values and the proper motion values. This might be attributed to the smaller sample of DFs, and the fact that only DFs perpendicular to the line of sight has been measured in this thesis. The data in Langangen et al. (2008b), are also obtained from a larger active region.

Langangen et al. (2008a)

The mean properties and corresponding standard deviations of the 26 Ca II λ8862 DFs analyzed in this paper are listed in Table 4.3. Comparing these values with the Ca 8542 values in Table 3.1, it can be seen that the mean lifetimes are the same, but that they have different standard deviations. The maximum Doppler velocities and Doppler deceleration on the other hand, are quite different. The mean value for Ca 8542 maximum Doppler velocity is about half of the Ca II λ8862 mean value, and the Ca 8542 mean Doppler deceleration value is about one third of the corresponding Ca II λ8862 mean value. Part of this discrepancy must be attributed to the different techniques of obtaining the Doppler measurements. This paper used the fitting of a linear line to the diagonal signatures of DFs in λ-T plots, while the Doppler measurements from this thesis used the shifts in the line profiles obtained from the DF paths. Higher Doppler values might have been obtained by investigating the spectral information of the more "static" part of the FOV of the data from the thesis, where the DFs presumably are more aligned along the line of sight. The difference in techniques might also be the reason that the values for Ca II λ8862 are more similar to proper motion values in Ca 8542.

Properties of the 26 Ca II λ8862 dynamic fibrils in Langangen et al. (2008a)	
Parameter	Mean
Lifetimes (min)	217 ± 39
Maximum Doppler velocities (km/s)	11.3 ± 3.8
Doppler decelerations (m/s^2)	89 ± 25

Table 4.3: Properties of the dynamic fibrils that have been analyzed in Langangen et al. (2008a). The mean values are shown, along with the standard deviation.

The scatter plots of this paper are based on Doppler measurements and shows strong correlation between the maximum velocities and the deceleration, and a weaker correlation between the DF durations and decelerations. This corresponds well with what was found for Ca 8542 for the Doppler measurements, and for the measurements derived from the parabola fit.

4.2 Conclusion and outlook

In this thesis, unique high spectral and spatial resolution images in H-α and Ca 8542 have been presented, from a 30 minute time series obtained with the CRISP instrument at the SST. From these observations, 50 dynamic fibrils have been identified and analyzed.

Analysis reveals evidence of parabolic motion of the dynamic fibrils in both spectral lines, indicating a possible evolution of the dynamic fibrils through the different chromospheric layers. The paths of the dynamic fibrils were generally much sharper and more clearly defined in H-α, possibly due to the difference in formation heights of the two lines, as well as the influence the transition region boundary may have in H-α formation.

The mean properties for dynamic fibrils measured in H-α and Ca 8542 are quite similar. The main differences are that dynamic fibrils in H-α appear to have larger maximum extensions or heights than Ca 8542, and that the Doppler measurements appear to have a larger spread for Ca 8542. These differences might be a result of the diffuseness of the DF in Ca 8542 and the more narrow line profile of the Ca 8542 line, respectively. The differences in proper motion values and Doppler values, are probably a consequence of the selection process. Additionally, the atmospheric conditions may have an effect also.

The values of the physical properties found for the 50 dynamic fibrils generally agree well with the values found from the literature studies discussed in this thesis. Correlations of the physical properties aligns well with the studies considered. Especially evident are the proper motion correlation of maximum velocities and decelerations and the Ca 8542 Doppler correlation of maximum velocities and decelerations. Earlier, these correlations have formed the basis for the conclusion that dynamic fibrils are driven by shock waves.

It is clear that more research can be done with this data set. If this research were to continue, investigation of more dynamic fibrils could be carried out, with the implications of regional differences as a starting point. The IDL code could be expanded to find dynamic fibrils from X-T plots automatically, and other fitting profiles e.g. a Gauss curve or a Voigt profile, might be more suitable to fit the line profiles of the two spectral lines. Regarding the dynamic fibril properties, a possible time delay between the DFs in H-α and Ca 8542 might be interesting to investigate, as well as widths of the dynamic fibrils. For the widths, other DF literature can be used for comparison e.g. De Pontieu et al. (2007a). Another suggestion would be to examine the "full" lifetimes of the Ca 8542 DFs, with the addition of including measurements from the line wing positions. By investigating the SDO data aligned to the SST FOV, possible extension of dynamic fibrils higher up in the hotter outer solar atmosphere could be made.

Bibliography

J. W. Brault and H. Neckel. *Spectral Atlas of Solar Absolute Disk-averaged and Disk-Center Intensity from 3290 to 12510 Å, ftp://ftp.hs.uni-hamburg.de/pub/outgolng/FTS-Atlas*, 1987.

M. Carlsson. A computer program for solving multi-level non-LTE radiative transferproblems in moving or static atmospheres. *Uppsala Astronomical Observatory Reports*, 33, 1986.

J. de la Cruz Rodríguez. *Measuring the solar atmosphere*. PhD thesis, Stockholm University, 2012.

B. De Pontieu, R. Erdélyi, and S. P. James. Solar chromospheric spicules from the leakage of photospheric oscillations and flows. *Nature*, 430:536–539, July 2004.

B. De Pontieu, V. H. Hansteen, L. Rouppe van der Voort, M. van Noort, and M. Carlsson. High-Resolution Observations and Modeling of Dynamic Fibrils. *ApJ*, 655:624–641, January 2007a.

B. De Pontieu, S. McIntosh, V. H. Hansteen, M. Carlsson, C. J. Schrijver, T. D. Tarbell, A. M. Title, R. A. Shine, Y. Suematsu, S. Tsuneta, Y. Katsukawa, K. Ichimoto, T. Shimizu, and S. Nagata. A Tale of Two Spicules: The Impact of Spicules on the Magnetic Chromosphere. *Publications of the Astronomical Society of Japan*, 59:655, November 2007b.

B. De Pontieu, S. W. McIntosh, V. H. Hansteen, and C. J. Schrijver. Observing the Roots of Solar Coronal Heating-in the Chromosphere. *ApJ*, 701:L1–L6, August 2009.

J. M. Fontenla, E. H. Avrett, and R. Loeser. Energy balance in the solar transition region. I - Hydrostatic thermal models with ambipolar diffusion. *ApJ*, 355:700–718, June 1990.

V. H. Hansteen, B. De Pontieu, L. Rouppe van der Voort, M. van Noort, and M. Carlsson. Dynamic Fibrils Are Driven by Magnetoacoustic Shocks. *ApJ*, 647:L73–L76, August 2006.

L. Heggland, B. De Pontieu, and V. H. Hansteen. Numerical Simulations of Shock Wave-driven Chromospheric Jets. *ApJ*, 666:1277–1283, September 2007.

T. Kosugi, K. Matsuzaki, T. Sakao, T. Shimizu, Y. Sone, S. Tachikawa, T. Hashimoto, K. Minesugi, A. Ohnishi, T. Yamada, S. Tsuneta, H. Hara, K. Ichimoto, Y. Suematsu, M. Shimojo, T. Watanabe, S. Shimada, J. M. Davis, L. D. Hill, J. K. Owens, A. M. Title, J. L. Culhane, L. K. Harra, G. A. Doschek, and L. Golub. The Hinode (Solar-B) Mission: An Overview. *Solar Physics*, 243: 3–17, June 2007.

M. L. Kutner. *Astronomy: A Physical Perspective*. Cambridge University Press, 2003.

Ø. Langangen, M. Carlsson, L. Rouppe van der Voort, V. Hansteen, and B. De Pontieu. Spectroscopic Measurements of Dynamic Fibrils in the Ca II λ8662 Line. *ApJ*, 673:1194–1200, February 2008a.

Ø. Langangen, L. Rouppe van der Voort, and Y. Lin. Measurements of Plasma Motions in Dynamic Fibrils. *ApJ*, 673:1201–1208, February 2008b.

J. Leenaarts, M. Carlsson, and L. Rouppe van der Voort. The Formation of the Hα Line in the Solar Chromosphere. *ApJ*, 749:136, April 2012.

J. R. Lemen, A. M. Title, D. J. Akin, P. F. Boerner, C. Chou, J. F. Drake, D. W. Duncan, C. G. Edwards, F. M. Friedlaender, G. F. Heyman, N. E. Hurlburt, N. L. Katz, G. D. Kushner, M. Levay, R. W. Lindgren, D. P. Mathur, E. L. McFeaters, S. Mitchell, R. A. Rehse, C. J. Schrijver, L. A. Springer, R. A. Stern, T. D. Tarbell, J.-P. Wuelser, C. J. Wolfson, C. Yanari, J. A. Bookbinder, P. N. Cheimets, D. Caldwell, E. E. Deluca, R. Gates, L. Golub, S. Park, W. A. Podgorski, R. I. Bush, P. H. Scherrer, M. A. Gummin, P. Smith, G. Auker, P. Jerram, P. Pool, R. Soufli, D. L. Windt, S. Beardsley, M. Clapp, J. Lang, and N. Waltham. The Atmospheric Imaging Assembly (AIA) on the Solar Dynamics Observatory (SDO). *Solar Physics*, 275:17–40, January 2012.

M. G. Löfdahl, M. J. van Noort, and C. Denker. Solar image restoration. In F. Kneer, K. G. Puschmann, and A. D. Wittmann, editors, *Modern solar facilities - advanced solar science*, page 119, 2007.

Tiago M. D. Pereira, Bart De Pontieu, and Mats Carlsson. Quantifying spicules. *ApJ*, 759(1):18, 2012.

W. D. Pesnell, B. J. Thompson, and P. C. Chamberlin. The Solar Dynamics Observatory (SDO). *Solar Physics*, 275:3–15, January 2012.

E. R. Priest. *Solar magneto-hydrodynamics*. D. Reidel Publishing Company, 1982.

L. Rouppe van der Voort, J. Leenaarts, B. de Pontieu, M. Carlsson, and G. Vissers. On-disk Counterparts of Type II Spicules in the Ca II 854.2 nm and Hα Lines. *ApJ*, 705:272–284, November 2009.

R. J. Rutten, F. C. M. Bettonvil, R. H. Hammerschlag, A. P. L. Jägers, J. Leenaarts, F. Snik, P. Sütterlin, K. Tziotziou, and A. G. de Wijn. The Dutch Open Telescope on La Palma. In A. V. Stepanov, E. E. Benevolenskaya, and A. G. Kosovichev, editors, *Multi-Wavelength Investigations of Solar Activity*, volume 223 of *IAU Symposium*, pages 597–604, 2004.

G. B. Scharmer. Comments on the optimization of high resolution Fabry-Pérot filtergraphs. *A&A*, 447:1111–1120, March 2006.

G. B. Scharmer, K. Bjelksjo, T. K. Korhonen, B. Lindberg, and B. Petterson. The 1-meter Swedish solar telescope. In S. L. Keil and S. V. Avakyan, editors, *Society of Photo-Optical Instrumentation Engineers (SPIE) Conference Series*, volume 4853 of *Society of Photo-Optical Instrumentation Engineers (SPIE) Conference Series*, pages 341–350, February 2003a.

G. B. Scharmer, P. M. Dettori, M. G. Lofdahl, and M. Shand. Adaptive optics system for the new Swedish solar telescope. In S. L. Keil and S. V. Avakyan, editors, *Society of Photo-Optical Instrumentation Engineers (SPIE) Conference Series*, volume 4853 of *Society of Photo-Optical Instrumentation Engineers (SPIE) Conference Series*, pages 370–380, February 2003b.

C. J. Schrijver and C. Zwaan. *Solar and Stellar Magnetic Activity*. Cambridge University Press, 2008.

A Secchi. *Le Soleil*, volume 2. Paris Gauthier-Villars, 1877.

D. H. Sekse, L. Rouppe van der Voort, and B. De Pontieu. Statistical Properties of the Disk Counterparts of Type II Spicules from Simultaneous Observations of Rapid Blueshifted Excursions in Ca II 8542 and Hα. *ApJ*, 752:108, June 2012.

M. Stix. *The sun : an introduction*. Springer, 2004.

A. Title and W.A. Rosenberg. Soup: Solar optical universal polarimeter. *Optical Engineering*, 20:815, 1981.

M. van Noort, L. Rouppe van der Voort, and M. G. Löfdahl. Solar Image Restoration By Use Of Multi-frame Blind De-convolution With Multiple Objects And Phase Diversity. *Solar Physics*, 228:191–215, May 2005.

J. E. Vernazza, E. H. Avrett, and R. Loeser. Structure of the solar chromosphere. III - Models of the EUV brightness components of the quiet-sun. *ApJ*, 45:635–725, April 1981.

G. Vissers and L. Rouppe van der Voort. Flocculent Flows in the Chromospheric Canopy of a Sunspot. *ApJ*, 750:22, May 2012.